Two FtsZ proteins orchestrate archaeal cell division through distinct functions in ring assembly and constriction

*Yan Liao[a.], *Solenne Ithurbide[a.], Jan Löwe[b.] and Iain G. Duggin[a.]

*These authors contributed equally.

a. The ithree institute, University of Technology Sydney, Ultimo, NSW, 2007, Australia.

b. MRC Laboratory of Molecular Biology, Francis Crick Avenue, Cambridge, CB2 0QH, UK.

Address correspondence to Iain G. Duggin (Iain.Duggin@uts.edu.au), Tel: +61 2 9514 8403.

Keywords: FtsZ, tubulin, archaea, cell division, cytokinesis, abiotic division, cell envelope, cell morphology.

Abstract

The tubulin homolog FtsZ assembles a ring in bacteria and plays a key role in the machinery that constricts to divide the cells. Many archaea encode two FtsZs from distinct families, FtsZ1 and FtsZ2, of previously unclear functions. We show that *Haloferax volcanii* cannot divide properly without either or both but proliferates in alternative ways via remarkable envelope plasticity. The FtsZs co-localize as a dynamic midcell division ring. FtsZ1 independently assembles and stabilizes FtsZ2 in the ring, and influences cell shape, whereas FtsZ2 functions in the constriction mechanism; their GTPase active sites are crucial for these activities. The two FtsZs are widespread in archaea with a single S-layer envelope, but those with a pseudomurein wall only have FtsZ1. FtsZ2 appears to be essential for constriction of the flexible membrane-S-layer, where an internal constriction force might dominate the division mechanism in contrast to bacteria and archaea that divide by wall ingrowth.

Introduction

To divide, a cell must first recruit the required molecular machinery in a ring-like assembly integrated with the cell envelope at the intended division site. It then initiates inward constriction of the ring that may be coupled to—or caused by—local synthesis of the envelope, leading to membrane severance and closure, and then cell separation. In bacteria, FtsZ is the most conserved cell division protein, and is the ancestral homolog of eukaryotic tubulins that form the microtubule cytoskeleton (Nogales et al., 1998). FtsZ is among the first molecules to assemble at the incipient division site, where it assembles into dynamic filaments lining the inside of the cytoplasmic membrane. Assembly requires additional regulators and factors that together create the ring-like structure around the cell, the Z-ring. The Z-ring acts as a scaffold to initiate recruitment of about a dozen core components required for cell division, although upward of ~30 factors appear to participate in or regulate division (Adams and Errington, 2009; Du and Lutkenhaus, 2017).

During the active phase of division, dynamic 'treadmilling' of FtsZ polymerization around the ring directs the synthesis of septal cell wall peptidoglycan to drive constriction (Bisson-Filho et al., 2017; Yang et al., 2017). This may be accompanied by a direct influence of FtsZ on membrane constriction (Osawa et al., 2008; Szwedziak et al., 2014). The peptidoglycan synthesis builds a septal wall between the two new cells, which splits to separate the two new cells in a process that is either continuous with septal wall synthesis and ring closure, or is activated after the septal cross-wall is complete (Typas et al., 2012; Zhou et al., 2015).

FtsZ and other members of the tubulin superfamily have been found throughout the domains of life, and can be grouped into three main branches: tubulins (primarily in eukaryotes), CetZ (archaea), and FtsZ (bacteria, archaea, and some eukaryotic organelles) (Aylett and Duggin, 2017; Vaughan et al., 2004). These globular proteins share the capacity to polymerize in a GTP-dependent manner to form filaments. Hydrolysis to GDP, which takes place at the interface between the polymer subunits, favors disassembly. Regulation of the location, timing and balance of this polymerization cycle drives accurate structural and positional changes at the cellular level (Löwe and Amos, 2009).

An *ftsZ* homolog was first identified in several archaea by DNA hybridization (Margolin et al., 1996; Wang and Lutkenhaus, 1996) and GTP-binding screens (Baumann and Jackson, 1996). The archaeal FtsZ showed GTPase activity *in vitro* (Wang and Lutkenhaus, 1996) and

was localized to mid-cell by immunofluorescence (Poplawski et al., 2000; Wang and Lutkenhaus, 1996). The first complete archaeal genome sequence, of *Methanocaldococcus jannaschii* (Bult et al., 1996), revealed multiple *ftsZ* homologs, whereas almost all bacterial genomes contain only one *ftsZ*. Some archaea do not contain FtsZ, including the phylum Crenarchaeota, where division is instead orchestrated by proteins related to the ESCRT-III complexes involved in membrane remodeling in eukaryotes (Lindas et al., 2008; Samson et al., 2008).

Many of the archaea that contain FtsZ have one or more additional tubulin-superfamily proteins from the CetZ family. The genome of the archaeal model organism *Haloferax volcanii* (Hartman et al., 2010) encodes eight tubulin-superfamily proteins—six CetZs, and two FtsZs. Work in *H. volcanii* showed that the CetZs were not individually required for division, but at least one is required for rod cell shape development (Duggin et al., 2015). In the same study, an FtsZ1-GFP fusion protein was observed to localize at midcell, and giant cells were seen upon expression of an FtsZ1 mutant affected in the GTPase domain. The results also suggested *H. volcanii* as an excellent model for archaeal cell biology, as it has relatively large and flat cells that show a variety of regulated morphologies and are well-suited to light and electron microscopy (Bisson-Filho et al., 2018; de Silva et al., 2020; Duggin et al., 2015). Furthermore, *H. volcanii* is easy to grow in a range of conditions and has well-established genetic tools (Pohlschroder and Schulze, 2019). Here we use *H. volcanii* to demonstrate that FtsZ1 and FtsZ2 have different functions in the mechanism of archaeal cell division.

Results

Two distinct clades of FtsZ in archaea

To identify features of the two archaeal FtsZ families and their distribution in well-known and recently discovered archaea, we surveyed the Archaea domain for the presence of FtsZ homologs in 60 complete or draft genomes of a diverse selection of species. This identified 149 non-redundant sequences from the broader tubulin superfamily, *i.e.* FtsZ, CetZ, tubulin, or other non-canonical relatives (Table S3). Molecular phylogenetic analysis (Fig. 1a) showed that archaeal FtsZ1, FtsZ2, and the well-studied bacterial/plant FtsZ form three distinct families that are approximately equally divergent from one another, whereas the CetZ family and various non-canonical sequences are more distant. Forty-nine of the surveyed genomes (including incomplete genomes) encode at least one FtsZ, 36 have at least two FtsZs, and 33 have at least one from each of the FtsZ1 and FtsZ2 families (Table S3). The dual-FtsZ arrangement therefore appears to be the most common in archaea and is present in diverse major taxa including most Euryarchaeota (*e.g.* Halobacteria, Thermococci and Archaeoglobi) and the DPANN and Asgard superphyla (Fig 1a). Interestingly, the five complete genomes analyzed from the archaeal phylum Methanobacteria and the one from Methanopyri have only one FtsZ each, which are positioned within the FtsZ1 family (Fig. 1a, Table S3). The Crenarchaeota and Thaumarchaeota lacked specific members of the FtsZ families. Thaumarchaeota contain several non-canonical tubulin-superfamily proteins that are unlikely to function in division (Aylett and Duggin, 2017), but as expected most Crenarchaeota do not contain any (Busiek and Margolin, 2011; Lindas et al., 2008; Samson et al., 2008). FtsZ was also not found in other species from *Candidatus* phyla Marsarchaeota and Verstraetearchaeota in the TACK superphylum, although FtsZ was identified in some other TACK groups such as Bathyarchaeota (Table S3).

H. volcanii FtsZ1 (HVO_0717) and FtsZ2 (HVO_0581) have the same overall domain arrangement as bacterial FtsZ. In the core fold of FtsZ, containing the GTP-binding and polymerization domains, the two *H. volcanii* FtsZs each shared high average sequence identity with other members of their respective families across the full diversity of archaea surveyed (Fig. 1b, percentages within each). Comparison of domains between the two *H. volcanii* proteins (Fig. 1b, %ID) showed lower sequence identity (46% overall), indicating conserved differences between the families. This was also seen by comparing average percent

identities amongst all proteins belonging to the archaeal FtsZ1, FtsZ2, and CetZ families (Table S4).

Closer inspection of the sequences revealed conserved differences between the families. An N-terminal extension (or 'N-tail') to the core fold is present in both FtsZ1 and FtsZ2 (Fig. 1b), confirming this region as a characteristic feature of the broader FtsZ family, compared to CetZ and tubulin that generally lack the N-tail. FtsZ1 and FtsZ2 have a conserved amphipathic amino-acid (aa) sequence of unknown structure at the very N-terminus (~9 aa), that appears to have similarity to the less conserved bacterial motif. FtsZ1 proteins then have an apparent spacer region (0-43 aa long, mean=21, SD=9, n=41) that shows poor sequence conservation but contains several proline and glycine residues, which are common in unstructured regions. This spacer is slightly longer on average than the corresponding charged region in FtsZ2 (0-18 aa long, mean=10, SD=5, n=35). Towards the C-terminal end of the N-tail, both archaeal FtsZs show a second amphipathic sequence (~8 aa) that is more conserved amongst FtsZ1 sequences, and forms an alpha helix (H0) in the previously determined crystal structure of *Methanocaldococcus jannaschii* FtsZ1 (Fig. 1d) (Löwe and Amos, 1998). Bacterial FtsZs appear to lack this N-tail spacer and second motif.

In the core domains, conserved differences between FtsZ1 and FtsZ2 were located in the vicinity of loops T4, T5, T6 and T7 in the N-terminal domain, which contribute to the GTP-binding interface located between subunits in FtsZ polymers (Fig. 1c-e) (Löwe and Amos, 1998; Nogales et al., 1998). In some regions, bacterial FtsZ showed conserved matches specifically to FtsZ1 and in other regions to FtsZ2, whereas some other sequence features were apparently specific to FtsZ1 or FtsZ2 (*e.g.* parts of the T7 loop region). Interestingly, the conserved T6-H6 amino acid triplet of FtsZ2 proteins ($DNN_{184\text{-}186}$ in HvFtsZ2) matched the equivalent region in eukaryotic tubulins and archaeal CetZs but differs from the triplet in bacterial FtsZ and archaeal FtsZ1 families (Fig. 1c).

The C-tail also varies in average length and sequence between the families (Fig. 1b). An initial variable region contains glycine and proline residues suggesting it may be another unstructured spacer (FtsZ1: 9-58 aa, mean=18, SD=10, n=41; FtsZ2: 10-78 aa, mean=37, SD=18, n=35), as seen in bacterial FtsZ (13-114 aa, mean=51, SD=24, n=25). A conserved ~6 aa motif is present near the end of the C-tail of FtsZ1 and FtsZ2, which differs from the ~10 aa bacterial FtsZ motif that plays a critical role in binding other division proteins (Du et al., 2015) (consensus: FtsZ=DDLDIPAFLR, FtsZ1=LGIDFV, FtsZ2=LGIDVI; Fig. 1c).

Since the conserved differences between archaeal FtsZ1 and FtsZ2 are primarily in the vicinity of the GTPase active site and longitudinal subunit interface (Fig. 1c-e), they are likely to reflect fundamental differences in the polymerization activities and functions of the two proteins.

Depletion of FtsZ1 or FtsZ2 causes division defects in H. volcanii

Given that *ftsZ* genes are nearly ubiquitous and important for survival in bacteria (Erickson and Osawa, 2010), we first aimed to construct and analyze *H. volcanii* strains that allow conditional repression of the expression of each *ftsZ* gene, in order to investigate the consequences on cells. We engineered strains in which expression of the genomic copy of the *ftsZ1* or *ftsZ2* gene was placed under the control of the highly specific tryptophan-regulated promoter *p.tna* (Large et al., 2007) (Fig. S1), so that the expression of each *ftsZ* could be maintained during strain construction and growth by the inclusion of tryptophan (Trp) in the growth medium, or depleted by placing the cells into medium without Trp. The two corresponding *H. volcanii* strains grew well in the presence of 2 mM Trp and appeared of approximately normal size and shape (Fig. 2a, 0 h, leftmost panels). However, resuspension of growing cells in liquid medium without Trp caused a large increase in cell size over the 24 h sampling period in both cases, as shown by phase contrast microscopy (Fig. 2a) and Coulter cytometry cell-volume distributions (Fig. S2). This signifies a defect in the regulation or mechanism of cell division in both the *ftsZ1*- and *ftsZ2*-depletion strains. The *ftsZ2* depletion resulted in significantly larger cells than *ftsZ1*-depletion, despite indistinguishable culture growth rates (Fig. 2a, S2), suggesting that the *ftsZ1*-depletion results in a lesser inhibition of division compared to the *ftsZ2*-depletion. Western blotting showed that the cellular amount of FtsZ1 decreased substantially over 6-9 h after withdrawal of Trp from the *p.tna-ftsZ1* strain (Fig. 2b, left panel). Whereas in the *p.tna-ftsZ2* strain, FtsZ2 had almost completely disappeared after 3 h (Fig. 2b, right panel). Hence, the milder cell division phenotype during FtsZ1 depletion might have been due to the differing rates or extents of depletion, or incomplete prevention of division by the loss of FtsZ1. We will address this uncertainty further below after we characterize the depletion phenotypes in more detail.

To observe the conformation and amount of genomic DNA in cells after FtsZ depletion, we stained cells (18 h after withdrawal of Trp) with SYTOX Green (SG) DNA stain, and then observed the cells by fluorescence microscopy and assessed relative cell size and DNA content by flow cytometry. The giant cells showed DNA-SG staining that appeared diffusely

present throughout the cytoplasm, similar to wild-type cells in terms of staining intensity and distribution throughout the cells (Fig. S3a). These observations were supported by flow cytometry, which showed that the DNA-SG fluorescence increased in correlation with the side-scatter signal as a proxy for cell size (Fig. S3b). Remarkably, some of the largest mutant cells (*e.g.* after *ftsZ2*-depletion) showed ~100-fold higher DNA-SG fluorescence and side-scatter than wild-type, corresponding to an expected genome copy number of ~2000 or more in the largest mutant cells, compared to the typical polyploidy of ~20 in unmodified *H. volcanii* (Breuert et al., 2006). These results indicate that DNA synthesis continues in approximate proportion to cell biomass increase during inhibition of cell division caused by FtsZ depletion, consistent with the previously observed correlation between DNA content and cell size in the wild-type *H. volcanii* division cycle (Delmas et al., 2013) (Fig. S3b).

We then used live-cell time-lapse microscopy of cells mounted on soft-agarose pads (containing growth medium) to visualize the cells from the start of FtsZ depletion. As may be seen in Fig. 2c and Video S1 (left panels), depletion of either FtsZ1 or FtsZ2 caused cells to enlarge significantly over time, a result of inhibition of division with ongoing cell growth. Some cells developed division constrictions near the start of the depletion but may not have been able to complete them (Fig. 2c). Later in the depletion, we also observed a budding-like process resulting in apparent vesicles or cell fragments of variable sizes (Fig. 2c, arrows, and Video S1). By imaging cells that had already been depleted in batch culture, we observed infrequent division in the giant FtsZ1-depleted cells, which sometimes resulted in a small cell fragment appearing at one side of the division plane during cell separation (Video S2); remarkably, fragments also rarely appeared to be ‘carved out’ from a cell edge. In contrast, FtsZ2 depleted cells were never seen dividing near midcell, although blebbing from cellular lobes of these very large cells was occasionally seen (Video S3).

FtsZ-depleted cells that were re-supplied with Trp at the commencement of time-lapse imaging (FtsZ restoration) showed that the giant cells then became capable of dividing (Fig. 2d, Video S1). Some underwent multiple simultaneous divisions, generating large cells that then underwent further division events to eventually re-establish a population of normal-sized cells. It was also clear that the division process itself was sometimes asymmetric (unilateral), where cell invagination occurs from only one edge (or predominately from one edge), and the plane of division was sometimes noticeably acentral, or not straight nor perpendicular to the cell envelope (Video S1). Irregular positioning of division sites may be expected based on the

sensitivity of division site positioning mechanisms to cell size and shape (Walsh et al., 2019), and they resulted in noticeable pleomorphology in the progeny.

H. volcanii propagates without FtsZ1 and/or FtsZ2

The above results demonstrated that division was closely linked to the expression of *ftsZ1* and *ftsZ2*. To investigate the relationship between *ftsZ* concentration and the efficiency of division, we established continuous mid-log cultures of the *p.tna-ftsZ1* and *p.tna-ftsZ2* strains at a range of Trp concentrations (from 0 to 2 mM Trp). These showed an inverse correlation between Trp concentration and cell size (Fig. S4a-b). We found that cultures of both *ftsZ*-depletion strains could be maintained indefinitely in standard growth medium (Hv-Cab) in the absence of added Trp. This suggested that the *ftsZ* genes might be individually non-essential for maintenance of cultures, or very low levels of each FtsZ produced in the absence of added Trp (Fig. S4c) were necessary and sufficient to support growth. We addressed these possibilities by employing the direct selection procedure (Allers et al., 2004) to individually delete the open reading frames of *ftsZ1* and *ftsZ2*. These strains were viable, and we also made the double-deletion strain (Δ*ftsZ1* Δ*ftsZ2*). All three deletion strains showed slower culture growth rates compared to the wild-type, and Δ*ftsZ1* Δ*ftsZ2* was slower than the single Δ*ftsZ* strains (Fig. 3a), with mean (±95% CI) OD_{600} doubling times of 3.08±0.06 h (wild-type H26), 3.58±0.27 h (Δ*ftsZ1*), 3.56±0.23 h (Δ*ftsZ2*) and 4.20±0.18 h (Δ*ftsZ1* Δ*ftsZ2*). Agar plating of mid-log samples (OD_{600} = 0.2) showed that the three Δ*ftsZ* strains had 20-25 fold fewer colony forming units (cfu) compared to the wild-type (Fig. S5a), consistent with a larger cell size (Fig. 3b, 3c) and/or a reduced fraction of viable cells in the three mutants.

During mid-log growth, the three deletion strains displayed very heterogeneously sized and misshapen cells, and a significant amount of cellular debris (< 1 μm^3, Fig. 3b-c), similar to the *ftsZ*-depletion strains when grown continuously without Trp (Fig. S4a). The Δ*ftsZ2* and Δ*ftsZ1* Δ*ftsZ2* strains showed more severe cell-division defects compared to Δ*ftsZ1*, consistent with depletion results, suggesting that FtsZ2 can provide a limited capacity for division in the absence of FtsZ1 (Fig. 3b-c). Also, the milder FtsZ1-depletion phenotype (Fig. 2a) was largely due to differing functions of FtsZ1 and FtsZ2 and not the differences in depletion rate (Fig. 2b). The apparent correlation between the appearance of greatly enlarged cells and debris (Fig. 3c) suggested that the largest cells produce cell fragments or disintegrate to form the debris. To investigate whether the 3D morphology of cells could help explain their striking shapes (Fig 3b) or how cell fragments and debris are produced (Fig. 3c),

Δ*ftsZ1* Δ*ftsZ2* cells were gently suspended in soft-agarose gel for 3D confocal microscopy (Fig. 3d, S5b, Video S4). The elongated cells showed a similar flattened shape profile as the wild-type rod- and plate-shaped cells, which are normally ~0.5 μm thick. However, the giant plate-like cells had lost much of the flatness of the wild-type, and displayed multi-lobed ramified 3D morphologies, underscoring the remarkable plasticity of the *H. volcanii* envelope in these giant cells.

To further assess the capacity of cells to survive without *ftsZ*, including potential propagation via alternative biotic processes, mid-log culture samples were transferred to soft-agarose media pads to image the cells during growth (Fig. 3e, S5c, Video S5-S8). Under these conditions, the mutants grew substantially larger over the recorded time-courses (~12 h), indicating that cells were structurally stabilized by the gel compared to the prior liquid culture (Fig. 3c). Nevertheless, while many Δ*ftsZ1* cells grew very large (Video S5), some occasionally divided, often very acentrally or with a crooked division plane (Video S6). Division was not seen in Δ*ftsZ2* cells, which expanded to extremely large sizes, and blebbing was rarely seen (Video S7). The Δ*ftsZ1* Δ*ftsZ2* strain showed large and misshapen plate-like cells, but long filamentous cells were also common (Fig. 3e, Video S8). These two categories of giant cells appear to be the result of division defects in the common plate and rods morphotypes, respectively. Interestingly, some filaments of Δ*ftsZ1* Δ*ftsZ2* showed substantial polar narrowing and extension (tubulation), followed by fission to produce much smaller fragments (Fig. 3f, Video S8). These samples also contained many small particles, consistent with debris seen in the Coulter cytometry results (< 1 μm^3; Fig. 3c), which may be the product of the polar tubulation-and-fission or fragmentation in prior culture. Overall, the fragmentation, budding, tubulation-and-fission, and, in the case of Δ*ftsZ1*, occasional inaccurate division, appears to help these cultures produce enough viable cells for propagation in the absence of normal cell division.

Reintroduction of each ftsZ in the corresponding deletion mutant recovers normal division

To determine whether the individual *ftsZ* open reading frames (ORFs) are directly responsible for the phenotypes observed in the respective deletion strains, we determined whether reintroduction of each *ftsZ* gene on a plasmid restored wild-type phenotype. To allow control of expression levels, the *ftsZ1* and *ftsZ2* ORFs were each placed under control of the *p.tna* promoter on the plasmid pTA962, and the two resulting plasmids were transferred to the Δ*ftsZ1* and Δ*ftsZ2* strains, respectively. Steady mid-log cultures were

established with different concentrations of Trp and cells were then observed by microscopy and Coulter cytometry. The Δ*ftsZ1* and Δ*ftsZ2* mutants harboring the vector only (pTA962) produced giant cells, consistent with the division defect of the original deletion strains (Fig. 3g, leftmost two panels). The strains containing the *ftsZ* expression plasmid in the corresponding *ftsZ* deletion strain showed normal cell sizes in the presence of 0.2 mM Trp induction or greater (Fig. 3g, S6a-b). At high concentrations of Trp (1 or 2 mM), the Δ*ftsZ1* + *ftsZ1* strain clearly showed some rods or spindle-like cell shapes (Fig. 3g, S6a), suggesting an influence of FtsZ1 overexpression on cell shape (investigated further below). Western blots confirmed that increasing Trp concentrations in cultures of Δ*ftsZ1* + *ftsZ1* resulted in increasing amounts of FtsZ1, and similarly, Δ*ftsZ2* + *ftsZ2* showed increasing levels of FtsZ2 (Fig. S6c); both proteins were effectively overproduced at the highest Trp levels. We conclude that the cell division phenotypes of the Δ*ftsZ1* and Δ*ftsZ2* strains are specifically caused by a lack of *ftsZ1* and *ftsZ2* expression, respectively.

Overexpression of ftsZ1 or ftsZ2 cannot properly compensate for loss of the other

We next sought to determine whether the cell division defect of each *ftsZ* knockout strain could be rescued by overexpressing the other FtsZ, i.e. by overexpressing FtsZ2 in the Δ*ftsZ1* strain, and vice versa in a cross-complementation experiment. If so, then this would indicate similar or overlapping functions of the two proteins. In the Δ*ftsZ1* strain containing a second copy of *ftsZ2* (in pTA962, under *p.tna* control) we observed weak complementation of the division defect in steady mid-log cultures containing Trp concentrations of 0.2 mM or greater (Fig. 3h). These cells were somewhat smaller than the Δ*ftsZ1* vector-only control but did not attain wild-type size as did Δ*ftsZ1* + FtsZ1 (Fig. 3g). Even at high Trp concentrations that cause greater protein overproduction (*e.g.* up to 2 mM Trp; Fig. S6c), cell size remained significantly larger in Δ*ftsZ1* + *ftsZ2* compared to the wild type (Fig. 3h, S7a, 7b). These findings show that the FtsZ2 overproduction cannot properly substitute for FtsZ1, but it may partially compensate for the missing FtsZ1, or have some capacity to take up some of the role(s) of FtsZ1 in division.

On the other hand, overproduction of FtsZ1 provided no detectable recovery from the Δ*ftsZ2* division defect (Fig. 3h, lower two panels; Fig. S6c, S7a), but caused somewhat greater heterogeneity of cell size (more debris) without specifically increasing the frequency of normal sized cells (Fig. S7b). Therefore, the FtsZ1 overproduction cannot substitute for loss of FtsZ2 in division. The Δ*ftsZ2* + *ftsZ1* strain showed some striking cell shapes, including

giant plate-like cells, some of which featured a spindle-like shape with rather pointy poles or various angular morphologies, and very long filamentous cells of approximately normal rod-cell width (Fig. 3h, S7a). The spindly cells therefore appear to be associated with FtsZ1 overproduction in both Δ*ftsZ1* and Δ*ftsZ2* backgrounds (compare Fig. 3g and 3h).

Overexpression of ftsZ1 or ftsZ2 cause contrasting phenotypes in a wild-type background

Our preceding results with Trp-controlled production of each FtsZ in the Δ*ftsZ* strains suggested that FtsZ1 and FtsZ2 likely have differing roles in cell division *in vivo*. If true, single overexpression of each FtsZ in the wild-type genetic background might exacerbate aspects of each protein's specific activities and potentially lead to different effects on cells, such as stimulation or inhibition of division. We found that FtsZ1 overproduction in the wild-type background during steady mid-log growth (i.e. H98 + pTA962-*ftsZ1*, with 2 mM Trp) resulted in larger cells than the vector-only control (Fig 4a, 4b), indicating that FtsZ1 overproduction leads to inefficient or misregulated division.

FtsZ1 overproduction also caused a change in cell shape, where cells frequently displayed a rod-like appearance or a noticeable taper at one or both poles (Fig. 4a and 4c). The results of *ftsZ1* overexpression are consistent with the effects observed with *ftsZ1* overexpression in the Δ*ftsZ* backgrounds (Fig. 3g, S6 and S7). In contrast, during *ftsZ2* overexpression (*i.e.* H98 + pTA962-*ftsZ2*, with 2 mM Trp), cells appeared as normal plates but were consistently smaller on average compared to the wild-type (Fig. 4a, 4b), indicating that FtsZ2 overproduction stimulates division. Western blotting confirmed the expected overproduction of FtsZ1 and FtsZ2 (~3 fold greater than wild type in each case; Fig. 4c). We conclude that overexpression of *ftsZ1* or *ftsZ2* leads to inhibition and stimulation of cell division, respectively, strongly supporting the notion that they have differing functions in cell division.

Different consequences of ftsZ1 and ftsZ2 mutations in stationary phase

The differing functions of FtsZ1 and FtsZ2 were also apparent when cultures of the knock-out, complementation and overexpression strains were compared in mid-log and stationary phases. Wild-type (H98 + pTA962) cells became smaller in stationary phase compared to mid-log, and this trend was also observed in the strains containing FtsZ2, *i.e.* Δ*ftsZ1*, Δ*ftsZ1* + *ftsZ1*, Δ*ftsZ1* + *ftsZ2*, and both overexpression strains (Fig. S8), in which almost wild-type cell sizes were attained in stationary phase. In contrast, the strains without FtsZ2 showed poor recovery from their cell division defects in stationary phase. These findings suggest that

FtsZ2 confers a partial ability to divide and recover more normal cell sizes as the cell growth rate slows in stationary phase, whereas cells without FtsZ2 have a much stronger block to division that is maintained even as cells slow or stop growth in stationary phase.

Predicted GTPase active site (T7 loop) residues are essential for FtsZ1 and FtsZ2 functions

FtsZ1 and FtsZ2 both contain the conserved GTP binding domain and catalytic residues in the T7 loop that are needed for GTP hydrolysis to occur in the FtsZ polymers (Fig. 1d). The GTPase activity is expected to be critical for the dynamic regulation of polymerization and therefore the function of FtsZ in the contraction of the division ring (Coltharp and Xiao, 2017; Nogales et al., 1998). Bacterial studies showed that point mutations of the T7 catalytic residues of FtsZ block GTPase-dependent filament disassembly, thus forming hyper-stable filaments that can co-assemble with the wild-type protein and severely disrupt function (Redick et al., 2005; Scheffers et al., 2001, 2002). Overexpression of an equivalent aspartate-to-alanine point mutant of FtsZ1 (D250A, substitution in the T7 loop) inhibited division in *H. volcanii* (Duggin et al., 2015).

To determine whether both FtsZ1 and FtsZ2 require their predicted GTPase catalytic residues for their functions in *H. volcanii* division, or whether these are partially or fully dispensable, we expressed *ftsZ1.D250A* and the equivalent *ftsZ2.D231A* mutant from plasmids (with 0.2 mM Trp) in their corresponding Δ*ftsZ* backgrounds. These mutants completely failed to complement the respective deletion strain's division defects, and appeared to exacerbate the phenotypes, particularly for FtsZ1 (compare Fig. 3b-c, 3i, S9b-c). Samples taken throughout the culture growth cycle confirmed that the Δ*ftsZ1* + *ftsZ1.D250A* strain formed giant misshapen plate-like cells, which became somewhat smaller as cells entered stationary phase, as well as substantial cell debris (Fig. S9a-c). Similarly, the Δ*ftsZ2* + *ftsZ2.D231A* strain displayed a mix of giant plates and cell debris, but also showed filaments (Fig. 3i), and tended towards somewhat smaller cells in stationary phase, with no very long filaments (Fig. S9d-f). These results show that the predicted T7-loop catalytic residues are essential for both FtsZ1 and FtsZ2 to function in division.

The apparent exacerbation of division defects by the point mutants suggested that they actively interfere with division or the envelope and could potentially have dominant-inhibitory effects in a wild-type cell context. Indeed, plasmid expression of *ftsZ1.D250A* or *ftsZ2.D231A* (with 0.2 mM Trp) caused strong division defects in the wild-type background

(Fig. S10). The cell size defects of *ftsZ1.D250A* expression became stronger at an elevated concentration of Trp (1 mM), whereas *ftsZ2.D231A* caused severe defects at both the lower (0.2 mM) and higher (1 mM) Trp concentrations (Fig. S10). These two mutants may therefore be used as powerful inhibitory tools in studies of *H. volcanii* cell biology. We next sought to investigate the assembly and subcellular localization of FtsZ1 and FtsZ2 in *H. volcanii*, and the consequences of the GTPase mutants on any localized assemblies.

Subcellular localization of FtsZ1 and FtsZ2

To investigate localization of FtsZ1 and FtsZ2, genes encoding fluorescent proteins, GFP and mCherry (mCh), fused to the C-termini of FtsZ1 and FtsZ2, were constructed for use in fluorescence microscopy. These fusions were initially tested for their ability to complement the corresponding deletion strain. FtsZ1-GFP or FtsZ1-mCh produced from plasmids (with 0.2 mM Trp) partially complemented the cell division defect of the Δ*ftsZ1* strain (Fig. S11a). Many cells showed normal size and shape with a fluorescent band at midcell or a division constriction, whereas others were larger and occasionally misshapen with more complex FtsZ1 structures near midcell. FtsZ2-GFP failed to complement the Δ*ftsZ2* division defect, but the highly filamentous cells did show sporadic FtsZ2-GFP bands (often ~3-4 μm from a pole) or foci (Fig. S11b).

Interference from fused fluorescent proteins is common in FtsZ and tubulin (Kimble et al., 2000; Moore et al., 2017; Sun and Margolin, 1998). Since the FtsZ fusion proteins were not fully functional in division as the sole copy, but did localize, we reasoned that they could be useful localization markers while not substantially perturbing cell division in the presence of the wild-type FtsZs as seen in bacteria. We found that low-level induction of FtsZ1 or FtsZ2 tagged with mCherry or GFP in a wild-type background resulted in normal cell size and shape. As may be seen in Fig 5a, FtsZ1-mCh localized as a band at midcell or the division constriction in almost all cells and cells showed no evidence of perturbed division at both 0.2 mM and 1 mM Trp (Fig. S11c). Similarly, cells producing FtsZ2-GFP displayed midcell or division constriction localization in almost all cells, which appeared normal or slightly enlarged with 0.2 mM Trp (Fig. 5b, S11d). With 1 mM Trp, cells producing FtsZ2-GFP were substantially enlarged and some had aberrant FtsZ2-GFP clusters near the center, consistent with their detachment from the envelope (Fig. 5b, S11d). The midcell bands of both proteins showed overall a very similar normalized distribution along the long axis (Fig. 5a-b, graphs) and both contracted with cell constriction (Fig. 5a-b, isolated cell images).

We confirmed the expected flattened ring-like structure of the midcell bands by imaging FtsZ1-GFP in the wild-type background with 3D structured-illumination microscopy (Fig. 5c, upper two images, ~70° xy tilt). This also revealed patchy, discontinuous or short helical structures (Fig. 5c, lower four images, ~20° xy tilt), generally comparable in appearance to bacterial Z-rings. Time-lapse imaging showed that the uneven fluorescence intensity of FtsZ1-GFP around the ring was dynamic during the cell cycle (Video S9, S10). These also clearly showed both unilateral and bilateral division of *H. volcanii*, as seen in enlarged cells (Video S1), and confirmed that prompt re-assembly of new rings occurs after division in locations consistent with cell morphology (Walsh et al., 2019). Video S9 also shows a rare cell in this strain that grows into a giant plate, showing a dynamic aster-like central cluster containing FtsZ1-GFP that was quite common in other giant plates (examples described further below).

Dual expression of FtsZ1-mCh and FtsZ2-GFP with 0.2 mM Trp caused no detectable cell size defect and only a mild effect with 1 mM Trp (Fig. 5d, S11e). As seen when separately produced, FtsZ1-mCh and FtsZ2-GFP appeared as a midcell band in essentially all cells (Fig. 5d), indicating that both proteins assemble into their midcell band very soon after the previous division, and remain approximately at midcell during growth. The co-localization correlation coefficient was > 0.8 in the majority of cells (Fig. 5d, lower right), reflecting a strong midcell co-localization but imperfect in some cells (Fig. 5d, lower panels; compare color intensity distributions in the cells). Both proteins then contracted together with constriction and remained generally co-localized during reassembly over several cell cycles (Fig. 5d, Video S11). The results in Fig. 5 show that the ring containing FtsZ1 and FtsZ2 closes down with division constrictions that range between unilateral to partially and equally bilateral.

Differing interdependency of FtsZ1 and FtsZ2 localization

The differing functions of FtsZ1 and FtsZ2 in division, and their co-localization at midcell, prompted us to investigate the dependency of FtsZ1 and FtsZ2 on each other for localization and assembly *in vivo*. We first produced each FtsZ-FP in the alternate Δ*ftsZ* strain. As may be seen in Fig. 6a, Δ*ftsZ2* cells producing FtsZ1-mCh (induced with 0.2 mM Trp) were mostly large and elongated as per the unlabeled Δ*ftsZ2* (Fig. 3g) and displayed one or more clear rings in most elongated cells. Rings occasionally appeared less condensed than normal or as a

short helicoid. Some giant plate-like cells were also present (not shown), which displayed central clusters containing FtsZ1-mCh (similar to the cluster in Fig. 6b and Video S9).

In contrast, FtsZ2-GFP (0.2 mM Trp) formed patches, foci and rarely short filaments, but no rings, in the Δ*ftsZ1* strain (Fig. 6a). Interestingly, this strain showed a much more severe division defect than Δ*ftsZ1* and Δ*ftsZ1* + unlabeled FtsZ2 (Fig. 3g, 3h), demonstrating that the GFP tag on FtsZ2 strongly inhibits the division by FtsZ2 in the Δ*ftsZ1* strains. Native FtsZ2 presumably assembles some form of ring to promote division in Δ*ftsZ1* cells, albeit inefficiently, so we used the lowest induction levels of FtsZ2-GFP in Δ*ftsZ1* (0 or 50 μM Trp), and indeed observed more filaments and occasional weak or poorly-formed rings that appeared more normal in constricting cells (examples in Fig. 6a - right-insets, and Fig. S12). Since FtsZ2-GFP induced with 0.2 mM Trp had only a very minor or undetectable effect on division when FtsZ1 is present in the wild-type background (Fig. 5b, S11d-e), and at higher levels (1 mM Trp) it inhibited division and appeared to inhibit envelope association (Fig. S11d), FtsZ1 must counteract the destabilizing effect of FtsZ2-GFP on normal FtsZ2 assembly. Taken together, the above data strongly suggest that FtsZ1 assembles independently, promotes proper FtsZ2 ring assembly at the midcell envelope, and stabilizes the FtsZ2 ring in cell division.

Next, we aimed to assess the degree of localization interdependence by specifically altering the assembly of each *ftsZ* and visualizing its influence on the other one. We expressed each *ftsZ* T7-loop mutant in the corresponding knockout and wild-type backgrounds, expecting them to produce aberrant hyper-stable polymers and strongly inhibit division (Fig. S10), and we simultaneously expressed a supplementary copy of the alternate fluorescent-tagged FtsZ.

When FtsZ2.D231A was produced as the sole copy of FtsZ2 (*i.e.* Δ*ftsZ2* background) with FtsZ1-mCh, highly elongated cells were observed, similar to the unlabeled strain, showing multiple FtsZ1-mCh rings or filaments (Fig. 6b, 3i). FtsZ1-mCh also appeared as helical structures (longer and more common than in Fig. 6a) or a broader zone of localization (Fig. 6b). The less frequent giant plates only rarely displayed a ring spanning the cell (*e.g.* Fig. 6b, lower right plate-like cell), likely due to a lack of spatial cues for positioning the division machinery in the giant malformed cells (Walsh et al., 2019) and a low probability of assembling a ring of such abnormal size. FtsZ1-mCh was more frequently seen as separate filaments or diffuse clusters in giant plates. These observations (Fig. 6b) suggest that FtsZ2.D231A has an influence on the proper condensation of FtsZ1 rings.

When FtsZ1.D250A was produced as the sole copy of FtsZ1 (Fig. 6b, right), the cells formed giant plates as expected, and FtsZ2-GFP most commonly displayed patches and foci, but no rings (as in Δ*ftsZ1*, Fig. 6a). This may be expected, due to the inherent difficulty in assembling rings in giant plates, and the disruptive GFP tag on FtsZ2 (without FtsZ1 to stabilize it). In addition, some of the FtsZ2-GFP appeared as separate filaments (Fig. 6b, right inset), more obvious than in Δ*ftsZ1*, suggesting that these were induced by FtsZ1.D250A. Overall, the moderate influence of the sole T7-mutants on the other FtsZ's localization pattern (compared to the respective knockout background in Fig. 6a), suggests that the T7 mutants might not efficiently homo-polymerize, or not efficiently interact/interfere with the other FtsZ.

Interestingly, the T7 mutants had striking and revealing effects on the other FtsZ's localization in the wild-type background (Fig. 6c), where they can form mixed polymers with corresponding wild-type FtsZs (*e.g.* FtsZ2 and FtsZ2.D231A). In this setting, FtsZ2.D231A production partially inhibited division during constriction (Fig. 6c, left) because the elongated cells often displayed multiple incomplete constrictions, with FtsZ1-mCh rings or occasional irregular structures present at those sites. Large plate-like cells with partial constrictions often showed aberrant clusters of FtsZ1-mCh at the cell center or irregular midcell rings (Fig. 6c). Thus, in some cells, FtsZ1-mCh was somewhat diverted from its normal ring structure and localization by the aberrant FtsZ2, consistent with the moderate feedback by FtsZ2 on FtsZ1 localization seen in Fig. 6a and 6b. Furthermore, the inhibition of division during ring constriction by the additional FtsZ2.D231A strongly suggests a primary role for FtsZ2, and its GTPase activity, in the active process of constriction.

FtsZ1.D250A production in the wild-type background caused the formation of clear aberrant filaments containing FtsZ2-GFP (Fig. 6c, right). Remarkably, none of these were associated with cell division, as the filaments were orientated seemingly at random in the cells, the longer ones aligning with the longer cell axis, thus defying division-site positioning mechanisms (Walsh et al., 2019). We saw above that wild-type FtsZ1 stabilizes FtsZ2-rings and counteracts the destabilization caused by the GFP tag on FtsZ2 (Fig. 6a, S11d), and, similarly, here it clearly also stabilized aberrant filament assembly containing FtsZ2-GFP (compare Fig. 6b and 6c), allowing us to conclude that FtsZ2 is strongly dependent on FtsZ1 for its subcellular assembly and function. Furthermore, the absence of midcell localization before any evidence of constriction seen with the additional FtsZ1.D250A suggests a primary

role for FtsZ1, and its GTPase activity, in the assembly and structural maintenance of the division machinery.

FP-tagging of the T7-mutants suppresses their dominant-inhibitory phenotypes, yet reveals co-localization with wild-type ftsZs and independent filaments of FtsZ1

Based on the above findings, we sought to simultaneously visualize the T7-mutant and the alternate wild-type FtsZ to detect any co-assembly. We initially looked at the FP-tagged T7-mutants individually. These proteins failed to complement their respective knockout strains, and they localized weakly as foci or very short filaments (Fig. S13a-b). Surprisingly, we found that the tags almost completely suppressed the strong dominant-inhibitory effects of the T7 mutations in the wild-type background; the cell size had returned almost to normal, yet the proteins still localized (Fig. 6d). FtsZ2.D231A-GFP showed apparently normal midcell localization and caused a substantially milder inhibition of division than FtsZ2-GFP at 1 mM Trp (S11d, S13d). Similarly, FtsZ1.D250A-mCh caused minimal disturbance to division and showed some midcell localization, but it also produced frequent aberrant filaments, clusters, and less distinct assemblies away from midcell (Fig. 6d, right). At 1 mM Trp, there were more noticeable cell deformations and protrusions, and small extracellular fluorescent particles (Fig. 6d, S13c). FtsZ1.D250A-mCh is clearly more independent of midcell than the more subservient FtsZ2.D231A-GFP. The simplest explanation for the above results is that the tagged T7-mutants form mixed filaments with the wild-type FtsZs that retain a capacity to localize without substantially disrupting the activity of the division machinery.

The two alternate combinations of the tagged T7-mutant and wild-type proteins were then transferred in dual-expression plasmids to the *ftsZ*-knockouts and wild-type *H. volcanii*. In Δ*ftsZ2* (Fig. 6e, left), FtsZ1-mCh localized in broad zones or lengthy helicoidal structures at intervals along the elongated cells. This suggests that the GFP on FtsZ2.D231A-GFP causes additional disruption to FtsZ1 condensation (compare to Fig. 6a, 6b). FtsZ2.D231A-GFP localized as foci (as did FtsZ2-GFP in *ftsZ* knockouts; Fig. 6a-b, S11b) that co-localized with patches of FtsZ1-mCh at similar intervals (Fig. 6e, left, inset). Similar results were seen in Δ*ftsZ1* Δ*ftsZ2*, but with weaker FtsZ1-mCh rings and helicoids (Fig. S13e). In Δ*ftsZ1* cells (Fig. 6e, right), FtsZ1.D250A-mCh and FtsZ2-GFP co-localized in patches around the edges of giant plates (compare to Fig. 6b, right). In addition, there were independent FtsZ1.D250A-mCh edge-patches. In Δ*ftsZ1* Δ*ftsZ2*, FtsZ1.D250A-mCh was similarly edge-associated and

thus minimally affected by the additional loss of FtsZ2 (Fig. S13e), but FtsZ2-GFP was diffuse with a few foci elsewhere, consistent with the requirement for wtFtsZ2 for normal FtsZ2-GFP localization (Fig. S11).

In the wild-type background (Fig. 6f), FtsZ1-mCh and FtsZ2.D231A-GFP both localized at midcell, and the cells were normal size and shape, consistent with the minimally disruptive behavior of the two proteins individually (Fig. 5a, 6d). Only at 1 mM Trp did we see moderately aberrant localization (Fig. 6f, left inset), although cell size and shape were still not substantially affected. On the other hand, FtsZ1.D250A-mCh and FtsZ2-GFP generated a moderate cell division defect (Fig. 6f, right; severe at 1 mM Trp, inset), as expected for FtsZ2-GFP, and displayed remarkable co-localization as helical or extended filaments and some independent filaments with FtsZ1.D250A-mCh. Comparison of Fig. 6c, d and f (right panels) strongly suggests that the filaments containing FtsZ2-GFP are caused by their association with long aberrant filaments containing FtsZ1.D250A. Taken together with a comparison of Fig. 6a, b and e (left panels), the data strongly support the view that: (1) FtsZ1 localization is largely independent of FtsZ2, (2) FtsZ2 assembly, positioning and stabilization are heavily dependent on the presence, localization and correct functioning of FtsZ1, and (3) FtsZ1-ring condensation (via a helicoid intermediate) is in turn promoted by feedback from the correct functioning of FtsZ2.

Discussion

This study has shown that archaeal FtsZ1 and FtsZ2, from distinct families within the tubulin superfamily of cytoskeletal proteins, are both involved in cell division and have different mechanistic roles. The specific consequences of mutations or overexpression of each protein and the subcellular assembly of the two FtsZs as a ring at the midcell division site clearly demonstrated that they are functionally and spatiotemporally involved in cell division *in vivo*. Remarkably, they were not essential for propagation in solid or liquid culture media and alternative types of division or abiotic fragmentation took place, mainly attributed to a surprising degree of envelope plasticity. FtsZ1 and FtsZ2 were able to form independent assemblies and rings of greatly differing stabilities—FtsZ1 rings were much sharper and more stable than FtsZ2 rings. FtsZ1 showed substantially more influence over FtsZ2 assembly, stability and correct localization than the converse, whereas FtsZ2 was specifically required for constriction.

H. volcanii cells deprived of FtsZ1 or FtsZ2 continued to grow and synthesise DNA (indefinitely) but could not divide efficiently or at all, resulting in giant and elongated cells (Fig. 2-3, S2-S6). This is morphologically comparable to the classical bacterial filamentous phenotype signifying inhibition of cell division (Slater and Schaechter, 1974). Interestingly, we also found that *H. volcanii* Δ*ftsZ1* Δ*ftsZ2* can be cultured indefinitely in standard conditions with solid or liquid media (Fig. 3). FtsZ is thought to be essential for division and survival in almost all walled bacteria (Erickson and Osawa, 2010), but under specific conditions of wall removal ('L-forms') or excess envelope—causing cell ramification—they can produce fragments and propagate without FtsZ (Leaver et al., 2009; Mercier et al., 2016). Similarly, *H. volcanii* Δ*ftsZ* strains can form giant ramified cells (Fig. 3). Most archaea, including *H. volcanii*, have a lipid membrane and a flexible glycoprotein S-layer but no cell wall (Albers and Meyer, 2011). Considering the morphological plasticity Δ*ftsZ* (Fig. 3, Video S1-S8) and wild-type *H. volcanii* (de Silva et al., 2020), a turbulent liquid environment may be expected to promote physical fragmentation or disintegration of the giant cells ('abiotic division'), from which any particles with a complete genome may be viable and contribute to propagation without proper cytokinesis (Fig. S3). Budding and polar tubulation-fission might also contribute to survival (Fig. 3, Video S1-S8). Similar non-FtsZ modes of proliferation can occur in wall-less bacteria (Abdelrahman et al., 2016; Errington, 2013; Lluch-Senar et al., 2010; Rivas-Marin et al., 2020). Our findings indicate that *H. volcanii*, and potentially other wall-less archaea, would be suitable for studying alternative division modes and the normal

cellular functions underpinning them, as well as abiotic division (Fig. 3) that could have helped sustain very early life on earth.

The archaeal cell division defect was consistently milder in cells lacking FtsZ1 compared to those lacking FtsZ2, and both situations can be completely rescued by expressing the corresponding *ftsZ* ORF (Fig. 3, 4, S8). This indicates that FtsZ2 can contribute to division, albeit inefficiently, in the absence of FtsZ1. Furthermore, FtsZ2 overproduction partially compensated for the lack of FtsZ1, improving division, whereas FtsZ1 overproduction failed to improve division in the absence of FtsZ2 (Fig. 3, S7), suggesting that the overproduced FtsZ2 could substitute for some of the functions normally carried out by FtsZ1—most likely the promotion of FtsZ2's activity or assembly into a functional ring. Consistent with this, FtsZ2 overproduction also stimulated division in the presence of FtsZ1 in the wild-type background, whereas FtsZ1 overproduction partially inhibited division (Fig. 4), indicating that the division stimulation is mainly caused by elevated activity of FtsZ2-specific functions. The overproduced FtsZ1 may decoy or interrupt the normal assembly and function of the division machinery. These findings suggest that FtsZ1 has a regulatory or recruitment/stabilization role that supports FtsZ2's direct function in effecting division.

We observed FtsZ1 and FtsZ2 dynamically assembling and co-localizing as a midcell ring soon after the previous division cycle, and then closing down with cell constriction later in the cell cycle, consistent with their continued coordination of functions during cell division (Fig. 5, Video S9-S11). The range of constrictions observed—from unilateral to evenly bilateral—suggests that the division mechanism and envelope are more flexible and subject to fluctuations in cell structure or external forces than walled bacteria that show robust uniform ingrowth. By mutating each FtsZ in different ways and observing the localization of the other, we discovered that FtsZ1 ring formation is not dependent on FtsZ2 (Fig. 6a). However, we infrequently observed FtsZ1 helicoid or incompletely condensed filaments instead of rings in the FtsZ2 knockout, and these structures appeared more prevalent in this strain producing a dominant-inhibitory FtsZ2 GTPase mutant (FtsZ2.D231A) and more obvious with the tagged mutant (FtsZ2.D231A-GFP) (Fig. 6a, 6b, 6e). That the FtsZ2 mutants can interfere with the condensation of FtsZ1 into rings supports the view that the two proteins are part of the same overall division complex (Fig 5). Importantly, FtsZ2.D231A inhibited division in the wild-type background, and cells showed multiple partial constrictions with rings containing FtsZ1-mCh (Fig. 6c). This strongly suggests that

FtsZ2.D231A efficiently co-assembles with wild-type FtsZ2 and specifically inhibits the constriction process. Taken together with our observation of FtsZ2-specific stimulation of constriction described above (Fig. 3, 4), we conclude that the primary function of FtsZ2 is to directly contribute to the division constriction mechanism in *H. volcanii*.

In contrast, we found that FtsZ2 ring formation is highly dependent on FtsZ1 (Fig. 6a). Occasional FtsZ2 rings observed in the absence of FtsZ1 were poorly formed and diffuse (Fig. 6a, S12), yet could lead to partially functional division. Furthermore, by modifying FtsZ1 localization through production of the dominant-inhibitory FtsZ1 GTPase mutant (FtsZ1.D250A), we saw the FtsZ2 localization is subservient to the independent behaviour and aberrant localization of the FtsZ1.D250A (Fig. 6b-f). Most strikingly, FtsZ1.D250A in the wild-type background strongly inhibited division with no evidence of partial constrictions and fairly straight filaments containing FtsZ2 were seen in apparently random orientations that beared no clear association with a potential midcell division plane (Fig. 6c). This strongly suggests that FtsZ1.D250A efficiently co-assembles with wild-type FtsZ1 and specifically inhibits normal localization of FtsZ1 and FtsZ2 before any constriction. Combined with the observations that FtsZ1 condenses and assembles the form of the ring (containing FtsZ2), and counteracts ring destabilization by FtsZ2-GFP to rescue division (Fig. 6a, S11, S12), we conclude that the primary function of FtsZ1 in cell division is to direct the stable assembly of the functional division ring (containing FtsZ2) and help maintain its stability during constriction.

Our results also revealed that FtsZ1 overproduction stimulated the formation of both rod and irregular-spindle (tapered) shaped cells instead of the common plate morphotype (Fig. 3g, 4), and similarly in the Δ*ftsZ* backgrounds (Fig. 3h, S7a). *H. volcanii* rods (but not spindles) also form during CetZ1 overproduction, and CetZ1 can also localize at midcell or as filaments along the cell edge perpendicular to the division plane during its key function in rod development (Duggin et al., 2015), suggesting a possible linkage between FtsZ1 and CetZ1 function in promoting cell elongation. Furthermore, nascent S-layer glycoprotein (SLG) and the PssA/PssD/ArtA enzymes required for its lipid modification were recently found to localize at midcell, and blocking this pathway caused rod formation but did not affect division (Abdul-Halim et al., 2020). These findings suggest a hypothesis in which FtsZ1 creates an independent scaffold at midcell, acting as a hub or landmark to recruit and stabilize the division, shape and envelope biosynthesis machineries.

FtsZ2 overproduction stimulated division but did not generate rods/spindles (Fig. 4), consistent with its specific role in division constriction. In bacteria, the constriction stage appears to be primarily driven by the FtsZ-directed ingrowth of the peptidoglycan cell wall (Bisson-Filho et al., 2017; Yang et al., 2017) and possibly an additional constriction force on the cytoplasmic membrane (Osawa et al., 2008; Szwedziak et al., 2014). However, with only a single flexible S-layer (a 2D semi-crystalline array), the *H. volcanii* envelope is almost certainly not capable of providing the same directionality or structural persistence that remodelling of the covalent peptidoglycan mesh would in bacterial septal ingrowth (Liao et al., 2018). FtsZ2 could be part of an alternative constriction-ratchet mechanism that enforces the inward directionality of constriction.

While the two FtsZs are conserved in the majority of surveyed archaea (Table S3), six of the 41 complete genomes encode only one FtsZ each. Remarkably, we noticed that the same six species, from the classes Methanobacteria and Methanopyri, are the only ones known to have a pseudomurein wall analogous to bacterial peptidoglycan (murein) (Table S3) (Steenbakkers et al., 2006; Visweswaran et al., 2011). Furthermore, in the current databases, these classes only encode FtsZ1 homologs. Electron microscopy of species from these classes show a clear septal wall during division (Burggraf et al., 1991; Zeikus, 1977; Zeikus and Wolfe, 1973), whereas species without pseudomurein only show a division furrow (Dobro et al., 2013; Mullakhanbhai and Larsen, 1975). The archaeal dual FtsZ system appears to have evolved after an early paralogous gene duplication and then FtsZ2 was lost when pseudomurein evolved in particular lineages. Our results and the clear phylogenetic association strongly suggest that FtsZ2 is required for constriction where there is no covalent wall ingrowth to impose directionality to division. We therefore predict that a division complex containing FtsZ2 provides an intrinsic constriction force and ratchet-like system for invagination of the flexible archaeal envelope that dominates the constriction mechanism in the absence of covalent cell wall ingrowth.

Interestingly, the unusual archaeon *Thermoplasma acidophilum* encodes two different, deep branching FtsZ sequences but no clear FtsZ2 (Fig. 1a, Table S3). *Thermoplasma* have a unique glycolipid envelope with no pseudomurein or S-layer (Huber and Stetter, 2006), raising the question of whether the unusual FtsZ pair in *Thermoplasma* evolved independently to play a role analogous to the common FtsZ1/2 system described here, or whether an alternative or additional cytoskeletal system exists for division (Makarova et al.,

2010). Other sporadic examples of multiple FtsZ or FtsZ-like proteins can be seen in archaea (Table S3) and bacteria, although the additional FtsZs appear not to function in division or have as yet unknown functions (Howell et al., 2019; Muller et al., 2014). Two plant FtsZ subfamilies within the major bacteria/plant family (Fig. 1a) are involved in division of plant plastids, and these FtsZs show functional differentiation during division of these multi-layered organelles derived from cyanobacteria (TerBush et al., 2013), raising the possibility that the plant and archaeal multi-FtsZ systems share some analogous activities related to division of a relatively flexible, multi-layered envelope.

Our study raises questions about how the two archaeal FtsZs are connected to the envelope at midcell and how they cooperate dynamically within the context of the division ring. FtsZ1 and FtsZ2 appear to independently associate with the envelope, although ring assembly of FtsZ2 is very weak without support from FtsZ1 (Fig. 6), so it is possible that their common features in the N- or C-terminal tails (Fig 1b), which show amphipathic characteristics that differ from the bacterial FtsZ tails, could be involved in direct membrane or adapter-protein binding. In bacteria such as *E. coli*, the actin homolog FtsA forms filaments that, together with ZipA and several regulatory or stabilization proteins, link FtsZ filaments to the membrane (Du and Lutkenhaus, 2017; Krupka and Margolin, 2018). However, homologs of these and most other bacterial and eukaryotic cell division proteins appear to be largely absent in archaea. One exception and likely candidate is the archaeal homolog of SepF, which can polymerize and participates with FtsA in anchoring FtsZ for Gram-positive bacterial division (Duman et al., 2013), and shows strong phylogenetic association with FtsZ in archaea (Makarova et al., 2010). Finally, at least some archaea including *H. volcanii* appear to utilize an intracellular spatial patterning system for division site placement, comparable to the bacterial Min system (Walsh et al., 2019), but the four MinD homologs in *H. volcanii* appear to have no substantial influence on division, and at least one is involved in polar positioning of the motility machinery instead (Nußbaum et al., 2020).

Given the functional differentiation of two FtsZs in archaeal cell division, and the corresponding lack of a cell wall, we propose that *H. volcanii* provides a powerful model for mechanistic studies of cell division to contrast against the well-studied bacterial models. We anticipate that this will contribute significantly towards establishing underlying principles of FtsZ-based division in all domains of life and help to unravel some of the mysteries of early cellular evolution.

Experimental Procedures

Identification, phylogeny and analysis of FtsZ sequences and structure

Thirteen known FtsZ protein sequences from bacteria and plants were aligned with MUSCLE (Edgar, 2004) for use as the search set to identify homologs in a diverse collection of 60 archaeal genomes (Table S3) by searching their respective Reference Proteome or UniProt databases using JackHMMER (Potter et al., 2018). All significant hits were selected, excluding several redundancies and low-quality sequences, and they were then aligned, together with the search set, using MUSCLE. The identification of homologs belonging to either the archaeal FtsZ1, FtsZ2, CetZ, or 'other' categories was done based on the position of individual sequences in a Maximum Likelihood phylogenetic tree, obtained using MEGA (ver. 7.0.26) (Kumar et al., 2018) with 100 bootstrap replicates, based on the alignment containing only those sites with >25% occupancy. *H. volcanii* FtsZ1 (HVO_0717), FtsZ2 (HVO_0581) and CetZ1 (HVO_2204) were taken as the reference sequences for identifying the three families.

To determine the percent sequence identities for each of the four domains, as defined for *H. volcanii* FtsZ1 and FtsZ2 in Fig. 1b, the sequence alignment generated above was arranged into protein families, including only those proteins classifying as FtsZ1, FtsZ2 or CetZ, and was then separated into individual domain alignments using Jalview (ver. 2.9.0b2) (Waterhouse et al., 2009). Each set was individually realigned with MUSCLE and used as input for generating a ClustalX percent identity matrix (Thompson et al., 2002) that was used for determining means. The crystal structure of *M. jannaschii* FtsZ1 (Löwe and Amos, 1998) (PDB code: 1FSZ) was displayed with PyMol (ver. 1.7).

Growth of H. volcanii

Most experimental *H. volcanii* cultures were grown in Hv-Cab medium (Duggin et al., 2015) or Hv-YPC medium for some genetic modification procedures (Allers et al., 2004). Where necessary as auxotrophic requirements, media were supplemented with uracil (10 µg/ml or 50 µg/ml) for Δ*pyrE2* strains, or thymidine and hypoxanthine (40 µg/ml each) for Δ*hdrB* strains. Cultures were incubated at 45°C with rotary shaking (200 rpm) and were generally maintained in continuous logarithmic growth (OD_{600} < 0.8) for at least 2 days prior to sampling for analysis of mid-log cultures, unless otherwise indicated. To control gene expression via the *p.tna* promoter, the indicated concentration of L-tryptophan (Trp) (Sigma), was included in these cultures.

Genomic modification

The strains used in this study and plasmids used to construct them as appropriate are listed in Tables S1 and S2, respectively. In order to generate strains allowing tryptophan-controlled expression of *ftsZ1* or *ftsZ2* for depletion studies (Fig. S1), two respective plasmids were first constructed that can recombine with each corresponding genomic *ftsZ* locus using two-step homologous recombination,(Allers et al., 2004) thereby substituting the normal transcriptional regulation of *ftsZ* with the specific tryptophan-inducible *p.tna* promoter. First, the upstream and downstream flanks for homologous recombination on either side of each *ftsZ* gene's start codon were PCR amplified from *H. volcanii* DS2 genomic DNA (upstream flank) and the corresponding pIDJL40-*ftsZ* plasmid (downstream flank, containing the L11e transcription terminator and *p.tna-ftsZ* cassette to be inserted), by using the primers given in Table S2. The upstream and downstream fragments in each case were joined, by overlap-extension PCR, and the products digested with HindIII and BamHI (sites located in the end primers; Fig. S1 and Table S2) and ligated to pTA131 (at HindIII-BamHI), giving pIDJL74 (*p.tna-ftsZ1*) and pIDJL75 (*p.tna-ftsZ2*). For *ftsZ1*, the sequence of the chosen upstream flank would result in a 39 bp deletion of genomic DNA immediately upstream of the *ftsZ1* start codon during the replacement. For *ftsZ2*, which is located as the second gene in a predicted operon (downstream of HVO_582, with a 2 bp gap), no genomic DNA was deleted when inserting the *p.tna* construct upstream of the *ftsZ2* ORF. To allow direct selection of the *p.tna-ftsZ* genomic replacements, the BamHI fragment from pTA1185 (T. Allers, personal communication), containing *p.fdx-hdrB* (Allers et al., 2004) was inserted at the BglII site in pIDJL74 and pIDJL75 (*i.e.* between the upstream and downstream fragments, described above). Clones containing the *p.fdx-hdrB* co-directional with the downstream *p.tna-ftsZ* cassette were selected and named pIDJL96 (*ftsZ1*) and pIDJL97 (*ftsZ2*) (Table S2).

Demethylated pIDJL96 and pIDJL97 (obtained via passage through *E. coli* C2925) were used to transform *H. volcanii* H98 separately, selecting isolated colonies that grew on agar medium (without uracil), which were expected to contain the plasmid integrated by single-crossover ("pop-in") (Allers et al., 2004) between the upstream or downstream flank and the corresponding genomic *ftsZ* locus. After growth of single colonies in liquid media (minus uracil), cells were plated onto Hv-Ca agar containing 10 μg/mL uracil, 50 μg/mL 5-fluoroorotic acid (FOA) and 0.5 mM Trp, to select for recombinational excision of these non-replicative plasmids ("pop-out") (Allers et al., 2004) that following gene conversion left the cassette containing *p.fdx-hdrB* and *p.tna-ftsZ* as the only copy of *ftsZ*; single colonies were

streaked onto the same medium, and then arising colonies were screened by allele-specific PCR to verify the expected chromosomal structure, giving strains ID56 (*p.tna-ftsZ1*) and ID57 (*p.tna-ftsZ2*) (Table S1).

To construct plasmids for deletion of each *ftsZ* gene, PCR fragments of downstream flanking DNA for *ftsZ*1 and *ftsZ2* were amplified (primers shown in Table S2). The products were digested with BglII and BamHI and then ligated respectively to the large fragments of pIDJL74 or pIDJL75 digested with BglII, BamHI and alkaline phosphatase. Isolated clones containing the appropriate co-orientation of up- and downstream flanks were selected and named pIDJL128 (*ftsZ1* flanks) and pIDJL129 (*ftsZ2* flanks) (Table S2). These plasmids were then digested with BglII (*i.e.* cutting between the flanks) and then the *p.fdx-hdrB* BamHI fragment from pTA1185 was ligated to them, generating pIDJL142 (for *ftsZ1* deletion) and pIDJL143 (for *ftsZ2* deletion).

To delete *ftsZ* and/or *ftsZ2* in *H. volcanii*, plasmids pIDJL142 and pIDJL143, respectively, were demethylated as described above, and then used to transform *H. volcanii* H98 using the two-step procedure noted above (Allers et al., 2004), yielding strains ID76 (i.e. (H98) Δ*ftsZ1-p.fdx-hdrB*), and ID77 (i.e. (H98) Δ*ftsZ2-p.fdx-hdrB*). Then, to construct the double-knock-out strain, *H. volcanii* ID77 was transformed with demethylated pIDJL128 (Table S2) using the two-step method described above, generating *H. volcanii* ID112. The expected mutations were verified by allele-specific PCR to detect both the presence of the expected *ftsZ*-deletion allele and the absence of the wild-type allele(s). In addition, the expected lack of the corresponding proteins was verified with western blotting using specific FtsZ1 or FtsZ2 antibodies (Fig. 2, S6c).

H. volcanii expression plasmids

All plasmids used are listed in Table S2. Plasmids pTA962 (Allers et al., 2010) or pIDJL40 (containing GFP) (Duggin et al., 2015) were used as the basis to construct plasmids for controlled expression of the *ftsZ* genes or modified versions. To construct pTA962-*ftsZ1*, the *ftsZ1* ORF (HVO_0717) was amplified from *H. volcanii* DS70 genomic DNA using primers *ftsZ1-f* and *ftsZ-r* (Table S2), and then the product was cloned between the NdeI and BamHI sites of pTA962. pTA962-*ftsZ2* was constructed in the same way, except with primers *ftsZ2-f* and *ftsZ2-r* to amplify the *ftsZ2* ORF (HVO_0581) (Table S2). The *ftsZ1.D250A* mutation was constructed previously (Duggin et al., 2015), and the *ftsZ2.D231A* mutation was

similarly made by overlap extension PCR using the mutational primers and primers *ftsZ2-f* and *ftsZ2-r* (Table S2) and the product cloned between NdeI and BamHI in pTA962.

The wild-type and mutant *ftsZ* ORFs were also amplified without their stop codons ('NS' primers; Table S2) and then cloned between the NdeI and BamHI sites of pIDJL40, to create *ftsZ-gfp* fusions (linker encoding GS, derived from the BamHI site). Then, to construct *ftsZ1-mCh* and *ftsZ2-mCh* fusions (pIDJL114 and pIDJL115, respectively), the GFP fragments in pIDJL40-*ftsZ1* and pIDJL40-*ftsZ2* were replaced by a BamHI-NotI fragment encoding a linker (GSAGSAAGSGEF, including the initial BamHI site and ending EcoRI site) and mCh (Table S2), as described previously (Duggin et al., 2015). To construct plasmids for expression of the mutant *ftsZ* genes tagged with mCh, NdeI + BamHI fragments (containing the point-mutant *ftsZ* genes without their stop codons) were ligated to the large fragment of pIDJL117 (*i.e.* expression of *cetZ1-mCh*) digested with NdeI and BamHI, thus replacing the *cetZ1* with the mutant *ftsZ* (Table S2). The expected DNA sequences of all cloned PCR products and point mutations in this study were verified by Sanger sequencing.

For dual expression of the various *ftsZ* genes, PvuII-fragments from the above plasmids (containing a *p.tna-ftsZ* gene fusion) were ligated into HindIII-cut (Klenow blunt-ended) plasmids containing the other *ftsZ* gene for the required combination, creating plasmids with two independent copies of the different *p.tna-ftsZ* fusions; the combinations made are given in Table S2, where the second-listed gene in the description refers to the one transferred secondarily in the PvuII fragment. All plasmids were demethylated by passage through *E. coli* C2925 and re-purified prior to transfer to *H. volcanii* by PEG-mediated spheroplast transformation (Allers et al., 2004).

Growth curves (microtiter plate) and colony (cfu) counting

Cultures maintained in log growth for at least 2 days were diluted to an OD_{600} of 0.005 with fresh medium, and then 150 µL volumes were dispensed into a BD Falcon 96-well culture plate per well. Absorbance (OD_{600}) of the samples over time was measured with a Tecan Spark 10M microplate spectrophotometer at 42°C with a orbital shaking (amplitude 2.5 mm, 216 rpm), with readings every 30 min for 56 h. Representative data from one of four independent experiments were then plotted, displaying standard error bars for technical replicates of the OD_{600} at each timepoint. Colony forming units (cfu) were determined by taking mid-log samples of each strain at OD_{600} = 0.2, and then plating 100 µL volumes of

serial dilutions onto Hv-Cab (+ 50 μg/mL uracil) agar, and colonies were then counted after 4-5 days incubation in a sealed bag at 45ºC.

Microscopy

For transmitted light and epifluorescence microscopy, a 1-2 μL sample of culture was placed on a 1% agarose pad containing 18% buffered saltwater (BSW) on a glass slide at room temperature, and a #1.5 glass coverslip was placed on top. Images were acquired using a 1.4 NA oil immersion objective with phase-contrast or differential-interference contrast transmission optics, or by epifluorescence with GFP (Ex: 475/28 nm; Em: 525/48 nm) or mCh (Ex: 632/22 nm; Em: 676/34 nm) filter sets. 3D structured-illumination microscopy (3D-SIM) was performed as previously described (Duggin et al., 2015).

For live-cell time-lapse imaging, the 'submerged-sandwich' technique was used (Duggin et al., 2015). Briefly, 1-2 μL of mid-log culture was placed on a ~1 mm thick gel pad (0.3% w/v agarose, containing the complete medium for the required conditions), that had been prepared on an 8 mm diameter #1.5 circular glass coverslip (WPI). The coverslip-pad-sample assembly was then lifted with forceps and placed, inverted, onto the base of a 35 mm glass-based (#1.5) FluoroDish (WPI). Three milliliters of pre-warmed liquid medium were then gently applied to cover the pad assembly on the base, and the lid was applied to avoid evaporation. Time-lapse imaging was performed at 45°C on a Nikon Ti-E microscope with a NA 1.45 oil-immersion phase-contrast objective, maintaining focus automatically during time-lapse.

For 3D confocal imaging, live cells were stained by addition of cytoplasmic vital stain Mitotracker Orange (1 μM) (Maslov et al., 2018) to mid-log cultures ~18 h (45°C with shaking) prior to washing the cells three times and resuspending in fresh medium (without stain), or by addition of membrane dye FM1-43 (5 μg/mL) to culture samples at 45°C for 15 min. The stained cells were then gently mixed with an equal volume of molten (45°C) 1% low-melting-point agarose in fresh growth medium, and the mixture was placed onto the base of a FluoroDish and the environment was maintained humidified with a wet tissue during imaging at 37 or 45°C. A Nikon A1 laser-scanning confocal microscope was used with a 488 nm laser z-step of 0.2 μm. Each 3D confocal series was deconvolved by NIS-elements software (Nikon) using blind deconvolution (20 iterations). The 3D volume visualization was rendered using depth-coded alpha blending to display the depth information, followed by the

blind deconvolution process for 20 iterations. The 3D video animations were created by rotation around Y-axis with a display rate of 20 frames per second.

Analysis of Cell circularity

Cell circularity image analysis was performed with MicrobeJ (Ducret et al., 2016) software in FIJI (Schindelin et al., 2012). Cells were automatically detected using 'bacteria' mode with the default morphology settings, and the edge correction algorithm was implemented to exclude non-cell particles. Abutting cells were separated by using the segmentation algorithm. The circularity of each cell was obtained by using the 'shape descriptors measurement' function. Cell circularity values (0-100%) were then used to generate a histogram.

Analysis of FtsZ1 and FtsZ2 subcellular localization

Fluorescent images were pre-treated with the background subtraction filter (ballsize = 8) in FIJI. FtsZ1 and FtsZ2 medial localization along the cell long axis were then done with MicrobeJ. Cell outlines were detected by phase-contrast image segmentation using the Otsu method, with medial axis mode, area > 0.98, and exclude-on-edges options, and then manually corrected where needed. FtsZ foci were detected using the 'Foci' and 'Smoothed' modes with a tolerance of 160, a Z-score of 8, and area > 0.005. Raw pixel intensities and medial profiles were recorded. Data were output using the MicrobeJ XStatProfile Plot function with the parameters: Stat: Median, Y axis: MEDIAL.intensity.ch1 (and 2 for colocalization), bin#:150 and then imported into GraphPad Prism (ver. 8) for graphing. The correlation coefficients for individual cells for FtsZ1 and FtsZ2 fluorescence were obtained using the MicrobeJ Statistic(s) function Stat.: count, Data: EXPERIMENT.count.total. Split horizontal: INTENSITY.ch2.correlation.ch1 and then exported to Prism to generate the frequency distribution.

Coulter and flow cytometry

For Coulter cytometry to obtain cell volume distributions, culture samples were diluted (1:100 or 1:1000) with 0.2-μm-filtered 18% BSW, and were analyzed with a Multisizer M4 Coulter cytometer (Beckman-Coulter) equipped with a 20 or 30 μm aperture tube, running and calibrated with 2 μm latex beads in 18% BSW as the electrolyte. Runs were completed in the volumetric mode (100 μL), with a current of 600 μA and gain of 4. For flow cytometry, mid-log culture samples were diluted 1:10 with a solution of 5 μM SYTOX Green in 18% BSW and incubated at room temperature for ~30 min before log-scale data acquisition

(triggered by a side-scatter threshold) with an LSR-II flow cytometer (BD) with 18% BSW as sheath fluid.

Western blotting

Rabbit antisera for detection of *H. volcanii* FtsZ1 and FtsZ2 were generated with a synthetic peptide antigen derived from the sequence of the C-terminal region of FtsZ1, (QAHAEERLEDIDYVE, Cambridge Research Biochemicals, UK), used at 1:1000 dilution of serum. For FtsZ2, antibodies were raised against a peptide containing an N-terminally derived sequence (ERQTQSSLEDSDDQFGDPR, Thermo Fisher, USA) (1:500 dilution of serum), and one derived from the C-terminal region (SDGGRDEVEKNNGLDVIR, Thermo Fisher, USA) (1:4000 dilution of affinity purified antibody stock of 2.95 mg/ml). The FtsZ2 antibodies were used either as diluted serum or affinity purified protein (selecting for binding for the target peptide), as follows. N-term (serum): Fig. 2b, S4c, S6c, and C-term (affinity purified): Fig. 4d.

H. volcanii cell pellets (carefully separated from any excess liquid medium) were resuspended in SDS–PAGE sample buffer and then the samples were heated (95°C, 5 min) and vortexed. Samples were separated by SDS-PAGE, and then electroblotted (Bio-Rad) on a nitrocellulose membrane (Protran, Whatman), and probed with the rabbit polyclonal primary antibodies described above, followed by secondary antibody (donkey anti-rabbit IgG-HRP, AbCam 16284, 1:5000 dilution), with standard techniques. Bands were detected by enhanced chemiluminescence reagents (Thermo Fisher), with an Amersham Imager 600 system.

Experimental replication

In addition to preliminary experiments carried out throughout this study, the data displayed are representative of at least two biological replicate experiments, and the displayed microscopy images and accompanying descriptions represent the whole sample dataset.

Acknowledgments

This study was supported by the Australian Research Council (FT160100010) and the UK Biotechnology and Biological Sciences Research Council (BBSRC) and Medical Research Council (MRC). We thank Chris Evenhuis, Lynne Turnbull, Michael Johnson and Louise Cole from the UTS Microbial Imaging Facility (MIF) for technical support.

Author Contributions

Designed research: ID, SI, YL, JL. Preliminary data and strain construction: ID, SI, YL. Contributed/analyzed data: Fig. 1: ID, Fig. 2: YL, Fig. 3: YL (b-i), SI (a), Fig. 4: YL, Fig. 5: SI (a-c), ID (d), Fig. 6: SI (a-f), YL/ID (a). Supplementary Figures: S1: YL/ID, S2: YL, S3: ID, S4: YL, S5: YL, S6: YL, S7: YL, S8: YL, S9: YL, S10: SI, S11: SI, S12: YL, SI, S13: SI. Supplementary Tables: S1: ID/SI, S2: ID/SI, S3: ID, S4: ID. Supplementary Videos: S1-S8: YL, S9-S10: ID, YL, S11: SI. Interpreted results, wrote and reviewed the manuscript: IGD, YL/SI, JL. Management, funding acquisition and supervision: IGD, JL.

Declaration of Interests

The authors declare no competing interests.

Supplementary Information

Supplementary videos, and a file containing supplementary tables, figures, video legends and references are available with the online version of this article.

References

Abdelrahman, Y., Ouellette, S.P., Belland, R.J., and Cox, J.V. (2016). Polarized Cell Division of *Chlamydia trachomatis*. PLoS pathogens *12*, e1005822.

Abdul-Halim, M.F., Schulze, S., DiLucido, A., Pfeiffer, F., Bisson Filho, A.W., and Pohlschroder, M. (2020). Lipid Anchoring of Archaeosortase Substrates and Midcell Growth in Haloarchaea. mBio *11*.

Adams, D.W., and Errington, J. (2009). Bacterial cell division: assembly, maintenance and disassembly of the Z ring. Nat Rev Microbiol *7*, 642-653.

Albers, S.V., and Meyer, B.H. (2011). The archaeal cell envelope. Nat Rev Microbiol *9*, 414-426.

Allers, T., Barak, S., Liddell, S., Wardell, K., and Mevarech, M. (2010). Improved strains and plasmid vectors for conditional overexpression of His-tagged proteins in *Haloferax volcanii*. Appl Environ Microbiol *76*, 1759-1769.

Allers, T., Ngo, H.P., Mevarech, M., and Lloyd, R.G. (2004). Development of additional selectable markers for the halophilic archaeon *Haloferax volcanii* based on the *leuB* and *trpA* genes. Appl Environ Microbiol *70*, 943-953.

Aylett, C.H.S., and Duggin, I.G. (2017). The tubulin superfamily in archaea. Sub-Cellular Biochemistry *84*, 393-417.

Baumann, P., and Jackson, S.P. (1996). An archaebacterial homologue of the essential eubacterial cell division protein FtsZ. Proceedings of the National Academy of Sciences of the United States of America *93*, 6726-6730.

Bisson-Filho, A.W., Hsu, Y.P., Squyres, G.R., Kuru, E., Wu, F., Jukes, C., Sun, Y., Dekker, C., Holden, S., VanNieuwenhze, M.S., *et al.* (2017). Treadmilling by FtsZ filaments drives peptidoglycan synthesis and bacterial cell division. Science *355*, 739-743.

Bisson-Filho, A.W., Zheng, J., and Garner, E. (2018). Archaeal imaging: leading the hunt for new discoveries. Molecular biology of the cell *29*, 1675-1681.

Breuert, S., Allers, T., Spohn, G., and Soppa, J. (2006). Regulated polyploidy in halophilic archaea. PLoS One *1*, e92.

Bult, C.J., White, O., Olsen, G.J., Zhou, L., Fleischmann, R.D., Sutton, G.G., Blake, J.A., FitzGerald, L.M., Clayton, R.A., Gocayne, J.D., *et al.* (1996). Complete genome sequence of the methanogenic archaeon, *Methanococcus jannaschii*. Science *273*, 1058-1073.

Burggraf, S., Stetter, K.O., Rouviere, P., and Woese, C.R. (1991). *Methanopyrus kandleri*: an archaeal methanogen unrelated to all other known methanogens. Syst Appl Microbiol *14*, 346-351.

Busiek, K.K., and Margolin, W. (2011). Split decision: a thaumarchaeon encoding both FtsZ and Cdv cell division proteins chooses Cdv for cytokinesis. Molecular microbiology *82*, 535-538.

Coltharp, C., and Xiao, J. (2017). Beyond force generation: Why is a dynamic ring of FtsZ polymers essential for bacterial cytokinesis? Bioessays *39*, 1-11.

de Silva, R.T., Abdul Halim, M.F., Pittrich, D.A., Brown, H.J., Pohlschroder, M., and Duggin, I.G. (2020). Improved growth and morphological plasticity of *Haloferax volcanii*. bioRxiv, 2020.2005.2004.078048.

Delmas, S., Duggin, I.G., and Allers, T. (2013). DNA damage induces nucleoid compaction via the Mre11-Rad50 complex in the archaeon *Haloferax volcanii*. Molecular Microbiology *87*, 168-179.

Dobro, M.J., Samson, R.Y., Yu, Z., McCullough, J., Ding, H.J., Chong, P.L., Bell, S.D., and Jensen, G.J. (2013). Electron cryotomography of ESCRT assemblies and dividing *Sulfolobus* cells suggests that spiraling filaments are involved in membrane scission. Molecular biology of the cell *24*, 2319-2327.

Du, S., and Lutkenhaus, J. (2017). Assembly and activation of the *Escherichia coli* divisome. Mol Microbiol *105*, 177-187.

Du, S., Park, K.T., and Lutkenhaus, J. (2015). Oligomerization of FtsZ converts the FtsZ tail motif (conserved carboxy-terminal peptide) into a multivalent ligand with high avidity for partners ZipA and SlmA. Mol Microbiol *95*, 173-188.

Ducret, A., Quardokus, E.M., and Brun, Y.V. (2016). MicrobeJ, a tool for high throughput bacterial cell detection and quantitative analysis. Nat Microbiol *1*, 16077.

Duggin, I.G., Aylett, C.H., Walsh, J.C., Michie, K.A., Wang, Q., Turnbull, L., Dawson, E.M., Harry, E.J., Whitchurch, C.B., Amos, L.A., *et al.* (2015). CetZ tubulin-like proteins control archaeal cell shape. Nature *519*, 362-365.

Duman, R., Ishikawa, S., Celik, I., Strahl, H., Ogasawara, N., Troc, P., Lowe, J., and Hamoen, L.W. (2013). Structural and genetic analyses reveal the protein SepF as a new membrane anchor for the Z ring. Proc Natl Acad Sci U S A *110*, E4601-4610.

Edgar, R.C. (2004). MUSCLE: multiple sequence alignment with high accuracy and high throughput. Nucleic acids research *32*, 1792-1797.

Erickson, H.P., and Osawa, M. (2010). Cell division without FtsZ--a variety of redundant mechanisms. Mol Microbiol *78*, 267-270.

Errington, J. (2013). L-form bacteria, cell walls and the origins of life. Open Biol *3*, 120143.

Hartman, A.L., Norais, C., Badger, J.H., Delmas, S., Haldenby, S., Madupu, R., Robinson, J., Khouri, H., Ren, Q., Lowe, T.M., *et al.* (2010). The complete genome sequence of *Haloferax volcanii* DS2, a model archaeon. PLoS One *5*, e9605.

Howell, M., Aliashkevich, A., Sundararajan, K., Daniel, J.J., Lariviere, P.J., Goley, E.D., Cava, F., and Brown, P.J.B. (2019). *Agrobacterium tumefaciens* divisome proteins regulate the transition from polar growth to cell division. Mol Microbiol *111*, 1074-1092.

Huber, H., and Stetter, K.O. (2006). Thermoplasmatales. In The Prokaryotes: Volume 3: Archaea Bacteria: Firmicutes, Actinomycetes, M. Dworkin, S. Falkow, E. Rosenberg, K.-H. Schleifer, and E. Stackebrandt, eds. (New York, NY: Springer New York), pp. 101-112.

Kimble, M., Kuzmiak, C., McGovern, K.N., and de Hostos, E.L. (2000). Microtubule organization and the effects of GFP-tubulin expression in *Dictyostelium discoideum*. Cell Motil Cytoskeleton *47*, 48-62.

Krupka, M., and Margolin, W. (2018). Unite to divide: Oligomerization of tubulin and actin homologs regulates initiation of bacterial cell division. F1000Res *7*, 235.

Kumar, S., Stecher, G., Li, M., Knyaz, C., and Tamura, K. (2018). MEGA X: Molecular Evolutionary Genetics Analysis across Computing Platforms. Mol Biol Evol *35*, 1547-1549.

Large, A., Stamme, C., Lange, C., Duan, Z., Allers, T., Soppa, J., and Lund, P.A. (2007). Characterization of a tightly controlled promoter of the halophilic archaeon *Haloferax volcanii* and its use in the analysis of the essential *cct1* gene. Mol Microbiol *66*, 1092-1106.

Leaver, M., Dominguez-Cuevas, P., Coxhead, J.M., Daniel, R.A., and Errington, J. (2009). Life without a wall or division machine in *Bacillus subtilis*. Nature *457*, 849-853.

Liao, Y., Ithurbide, S., de Silva, R.T., Erdmann, S., and Duggin, I.G. (2018). Archaeal cell biology: diverse functions of tubulin-like cytoskeletal proteins at the cell envelope. Emerg Top Life Sci *2*, 547-559.

Lindas, A.C., Karlsson, E.A., Lindgren, M.T., Ettema, T.J., and Bernander, R. (2008). A unique cell division machinery in the Archaea. Proceedings of the national academy of sciences of the United States of America *105*, 18942-18946.

Lluch-Senar, M., Querol, E., and Pinol, J. (2010). Cell division in a minimal bacterium in the absence of ftsZ. Mol Microbiol *78*, 278-289.

Löwe, J., and Amos, L.A. (1998). Crystal structure of the bacterial cell-division protein FtsZ. Nature *391*, 203-206.

Löwe, J., and Amos, L.A. (2009). Evolution of cytomotive filaments: the cytoskeleton from prokaryotes to eukaryotes. Int J Biochem Cell Biol *41*, 323-329.

Makarova, K.S., Yutin, N., Bell, S.D., and Koonin, E.V. (2010). Evolution of diverse cell division and vesicle formation systems in Archaea. Nat Rev Microbiol *8*, 731-741.

Margolin, W., Wang, R., and Kumar, M. (1996). Isolation of an *ftsZ* homolog from the archaebacterium *Halobacterium salinarium*: implications for the evolution of FtsZ and tubulin. J Bacteriol *178*, 1320-1327.

Maslov, I., Bogorodskiy, A., Mishin, A., Okhrimenko, I., Gushchin, I., Kalenov, S., Dencher, N.A., Fahlke, C., Buldt, G., Gordeliy, V., *et al.* (2018). Efficient non-cytotoxic fluorescent staining of halophiles. Sci Rep *8*, 2549.

Mercier, R., Kawai, Y., and Errington, J. (2016). Wall proficient *E. coli* capable of sustained growth in the absence of the Z-ring division machine. Nat Microbiol *1*, 16091.

Moore, D.A., Whatley, Z.N., Joshi, C.P., Osawa, M., and Erickson, H.P. (2017). Probing for Binding Regions of the FtsZ Protein Surface through Site-Directed Insertions: Discovery of Fully Functional FtsZ-Fluorescent Proteins. J Bacteriol *199*.

Mullakhanbhai, M.F., and Larsen, H. (1975). *Halobacterium volcanii spec. nov.*, a Dead Sea halobacterium with a moderate salt requirement. Arch Microbiol *104*, 207-214.

Muller, F.D., Raschdorf, O., Nudelman, H., Messerer, M., Katzmann, E., Plitzko, J.M., Zarivach, R., and Schuler, D. (2014). The FtsZ-like protein FtsZm of *Magnetospirillum gryphiswaldense* likely interacts with its generic homolog and is required for biomineralization under nitrate deprivation. J Bacteriol *196*, 650-659.

Nogales, E., Downing, K.H., Amos, L.A., and Lowe, J. (1998). Tubulin and FtsZ form a distinct family of GTPases. Nature Structural Biology *5*, 451-458.

Nußbaum, P., Ithurbide, S., Walsh, J.C., Patro, M., Delpech, F., Rodriguez-Franco, M., Curmi, P.M.G., Duggin, I.G., Quax, T.E.F., and Albers, S.-V. (2020). An oscillating MinD protein determines the cellular positioning of the motility machinery in archaea. bioRxiv, 2020.2004.2003.021790.

Osawa, M., Anderson, D.E., and Erickson, H.P. (2008). Reconstitution of contractile FtsZ rings in liposomes. Science *320*, 792-794.

Pohlschroder, M., and Schulze, S. (2019). *Haloferax volcanii*. Trends Microbiol *27*, 86-87.

Poplawski, A., Gullbrand, B., and Bernander, R. (2000). The *ftsZ* gene of *Haloferax mediterranei*: sequence, conserved gene order, and visualization of the FtsZ ring. Gene *242*, 357-367.

Potter, S.C., Luciani, A., Eddy, S.R., Park, Y., Lopez, R., and Finn, R.D. (2018). HMMER web server: 2018 update. Nucl Acids Res *46*, W200-W204.

Redick, S.D., Stricker, J., Briscoe, G., and Erickson, H.P. (2005). Mutants of FtsZ targeting the protofilament interface: effects on cell division and GTPase activity. J Bacteriol *187*, 2727-2736.

Rivas-Marin, E., Peeters, S.H., Claret Fernandez, L., Jogler, C., van Niftrik, L., Wiegand, S., and Devos, D.P. (2020). Non-essentiality of canonical cell division genes in the planctomycete *Planctopirus limnophila*. Sci Rep *10*, 66.

Samson, R.Y., Obita, T., Freund, S.M., Williams, R.L., and Bell, S.D. (2008). A role for the ESCRT system in cell division in archaea. Science *322*, 1710-1713.

Scheffers, D.J., de Wit, J.G., den Blaauwen, T., and Driessen, A.J. (2001). Substitution of a conserved aspartate allows cation-induced polymerization of FtsZ. FEBS Lett *494*, 34-37.

Scheffers, D.J., de Wit, J.G., den Blaauwen, T., and Driessen, A.J. (2002). GTP hydrolysis of cell division protein FtsZ: evidence that the active site is formed by the association of monomers. Biochemistry *41*, 521-529.

Schindelin, J., Arganda-Carreras, I., Frise, E., Kaynig, V., Longair, M., Pietzsch, T., Preibisch, S., Rueden, C., Saalfeld, S., Schmid, B., *et al.* (2012). Fiji: an open-source platform for biological-image analysis. Nature methods *9*, 676-682.

Slater, M., and Schaechter, M. (1974). Control of cell division in bacteria. Bacteriol Rev *38*, 199-221.

Steenbakkers, P.J., Geerts, W.J., Ayman-Oz, N.A., and Keltjens, J.T. (2006). Identification of pseudomurein cell wall binding domains. Mol Microbiol *62*, 1618-1630.

Sun, Q., and Margolin, W. (1998). FtsZ dynamics during the division cycle of live *Escherichia coli* cells. J Bacteriol *180*, 2050-2056.

Szwedziak, P., Wang, Q., Bharat, T.A., Tsim, M., and Lowe, J. (2014). Architecture of the ring formed by the tubulin homologue FtsZ in bacterial cell division. Elife *3*, e04601.

TerBush, A.D., Yoshida, Y., and Osteryoung, K.W. (2013). FtsZ in chloroplast division: structure, function and evolution. Curr Opin Cell Biol *25*, 461-470.

Thompson, J.D., Gibson, T.J., and Higgins, D.G. (2002). Multiple sequence alignment using ClustalW and ClustalX. Current protocols in bioinformatics / editoral board, Andreas D Baxevanis [et al] *Chapter 2*, Unit 2 3.

Typas, A., Banzhaf, M., Gross, C.A., and Vollmer, W. (2012). From the regulation of peptidoglycan synthesis to bacterial growth and morphology. Nat Rev Microbiol *10*, 123-136.

Vaughan, S., Wickstead, B., Gull, K., and Addinall, S.G. (2004). Molecular evolution of FtsZ protein sequences encoded within the genomes of archaea, bacteria, and eukaryota. J Mol Evol *58*, 19-29.

Visweswaran, G.R., Dijkstra, B.W., and Kok, J. (2011). Murein and pseudomurein cell wall binding domains of bacteria and archaea--a comparative view. Appl Microbiol Biotechnol *92*, 921-928.

Walsh, J.C., Angstmann, C.N., Bisson-Filho, A.W., Garner, E.C., Duggin, I.G., and Curmi, P.M.G. (2019). Division plane placement in pleomorphic archaea is dynamically coupled to cell shape. Mol Microbiol *112*, 785-799.

Wang, X., and Lutkenhaus, J. (1996). FtsZ ring: the eubacterial division apparatus conserved in archaebacteria. Mol Microbiol *21*, 313-319.

Waterhouse, A.M., Procter, J.B., Martin, D.M., Clamp, M., and Barton, G.J. (2009). Jalview Version 2--a multiple sequence alignment editor and analysis workbench. Bioinformatics *25*, 1189-1191.

Yang, X., Lyu, Z., Miguel, A., McQuillen, R., Huang, K.C., and Xiao, J. (2017). GTPase activity-coupled treadmilling of the bacterial tubulin FtsZ organizes septal cell wall synthesis. Science *355*, 744-747.

Zeikus, J.G. (1977). The biology of methanogenic bacteria. Bacteriol Rev *41*, 514-541.

Zeikus, J.G., and Wolfe, R.S. (1973). Fine structure of *Methanobacterium thermoautotrophicum*: effect of growth temperature on morphology and ultrastructure. J Bacteriol *113*, 461-467.

Zhou, X., Halladin, D.K., Rojas, E.R., Koslover, E.F., Lee, T.K., Huang, K.C., and Theriot, J.A. (2015). Bacterial division. Mechanical crack propagation drives millisecond daughter cell separation in *Staphylococcus aureus*. Science *348*, 574-578.

Figure Legends

Figure 1. Molecular phylogeny and comparison of archaeal FtsZ1 and FtsZ2 families. (a) Phylogenetic tree based on alignment of 149 tubulin-superfamily proteins encoded in a set of 60 diverse archaeal genome sequences (Table S3), with the bacterial and plant FtsZ sequences that were used to identify them. Statistical support for selected branches is given (bootstrap, %). The two archaeal FtsZ groups are defined by the presence of reference proteins from *H. volcanii* (HVO_0581 - FtsZ2 and HVO_0717 - FtsZ1). Some non-canonical deeply branching FtsZ-like sequences present in Thaumarchaeota, Korarchaeota and others of unknown function, as well as the CetZ family (involved in cell shape), were also identified. (b) Domain organization and percent sequence identities for FtsZ1 and FtsZ2. The percentages over the domains (green and purple boxes) indicate the average sequence identity in that region for each *H. volcanii* FtsZ compared to all of the other members of the same family that were identified across the Archaea domain. The region between FtsZ1 and FtsZ2 represents the percent identity in the region between the *H. volcanii* FtsZ1 and FtsZ2 (%ID). The approximate location of conserved sequence motifs within the tail regions are indicated by vertical bars, colored to indicate similarities between the two. (c) Aligned sequence regions containing conserved differences between the bacterial/plant FtsZ and the archaeal FtsZ1 and FtsZ2 families, labelled with the secondary structural elements (Nogales et al., 1998). Boxed residues indicate conserved sites that are displayed in panel (e). (d) Crystal structure of FtsZ1 from *Methanocaldococcus jannaschii* (PDB: 1FSZ) (Löwe and Amos, 1998), with selected loops (T4-T7) involved in nucleotide binding and hydrolysis shown in pink. GDP is shown in orange, and the main domains are colored as in panel (b). Boxed regions are expanded in panel (e), which displays some conserved residues that characteristically differ between the FtsZ1 and FtsZ2 families (grey space-filling models, with FtsZ2 consensus residues in parentheses) and cluster around the nucleotide-dependent polymerization surfaces.

Figure 2. Depletion of FtsZ1 or FtsZ2 results in defects in cell division. (a) Phase-contrast microscopy of samples from cultures (*H. volcanii* ID56 - *p.tna-ftsZ1*, and ID57 - *p.tna-ftsZ2*) at the indicated time-points after initiating depletion by withdrawal of Trp from the growth medium. Strains with the genomic *ftsZ* genes placed under the control of the *p.tna* promoter were initially maintained in log growth for 2 days in Hv-Cab medium with 2 mM Trp, and then cells were washed three times and resuspended in Trp-free medium, to give an OD_{600} of 0.25. Phase-contrast images were obtained immediately before washing (0 h) and after 3, 6, 9

and 24 h of incubation without Trp, as indicated (note: 24 h samples are in an early stationary phase; Fig. S2a). Scale bars are 5 µm. (b) Western blots probed with FtsZ1 or FtsZ2 antisera during depletion with the corresponding Ponceau S pre-staining of total protein. The separate wild-type (H26) samples were from the same blots. A double band was observed (esp. FtsZ2), suggesting a modified/clipped form of the protein forms during sample preparation or *in vivo*. (c) *In situ* time-lapse imaging of FtsZ depletion. Cells cultured in Hv-Cab + 2 mM Trp were washed and placed onto agarose media pads without Trp and imaged over time. Arrows indicate budding-like events observed in some cells during depletion. (d) *In situ* time-lapse imaging of FtsZ restoration. The respective *p.tna-ftsZ* strains were initially grown without Trp inducer, and then cells were washed and placed onto agarose media (Hv-Cab) pads including 0.2 mM Trp for FtsZ1, and 2 mM Trp for FtsZ2. Scale bars (c-d), 2 µm.

Figure 3. FtsZ1 and FtsZ2 are dispensable for survival but required for normal cell division. (a) Microtiter plate monitoring of growth (OD_{600}) of *H. volcanii* wild-type (H26), Δ*ftsZ1* (ID76), Δ*ftsZ2* (ID77), and Δ*ftsZ1* Δ*ftsZ2* (ID112), sampled during mid-log growth (OD_{600} = 0.2) in Hv-Cab medium (+ 50 µg/mL uracil). Scale bars, 5 µm. (b) Phase-contrast images and (c) Coulter cell-volume frequency distributions (normalized to total count) of the strains. (d) Confocal microscopy 3D-reconstructed images of *H. volcanii* wild-type (H98 + pTA962) and ID112 (Δ*ftsZ1* Δ*ftsZ2*) cells, stained with Mitotracker Orange and embedded in low melting point agarose. The reconstructions are shown with a ~45º rotation around the x-axis. The color scale indicates the z-depth, and the length scale bars (horizontal) are 2 µm. Similar morphologies were seen with other *ftsZ* mutants and FM1-43 membrane staining (Fig. S5b). (e) Live cell time-lapse images recorded at 2 h intervals of the Δ*ftsZ1* Δ*ftsZ2* strain growing on an agarose gel media pad (scale bar, 5 µm), and (f) showing polar tubulation and budding-like processes (1 h frame intervals, left to right) observed in Δ*ftsZ1* Δ*ftsZ2* filaments (scale bar, 5 µm). (g) Phase-contrast microscopy of the two Δ*ftsZ* strains containing expression plasmids, sampled in steady mid-log growth in Hv-Cab medium with the indicated concentrations of Trp. Left two panels: vector only (pTA962). Righthand four panels: self-complementation strains, ID86 (Δ*ftsZ1* + pTA962-*ftsZ1*) and ID92 (Δ*ftsZ2* + pTA962-*ftsZ2*). (h) Cross-complementation strains, ID87 (Δ*ftsZ1* + pTA962-*ftsZ2*) and ID91 (Δ*ftsZ2* + pTA962-*ftsZ1*), mid-log in Hv-Cab with 0.2 mM and 2 mM Trp. (i) *ftsZ*-deletion strains expressing the corresponding GTPase active-site (T7-loop) mutant (i.e. ID88, Δ*ftsZ1* + pTA962-*ftsZ1.D250A* and ID93, Δ*ftsZ2* + pTA962-*ftsZ2.D231A*), mid-log in Hv-Cab with 0.2 mM Trp. Scale bars (g, h, i) are 5 µm.

Figure 4. Overproduction of FtsZ1 or FtsZ2 differentially affects cell division and shape. (a) Phase contrast micrographs of *H. volcanii* wild-type (H98 + pTA962), ID25 (FtsZ1 overproduction, H98 + pTA962-*ftsZ1*) and ID26 (FtsZ2 overproduction strain, H98 + pTA962-*ftsZ2*) mid-log cultures in Hv-Cab + 2 mM Trp. Scale bars, 5 µm. (b) Coulter cell-volume frequency distributions (normalized to total count) of the strains in panel (a). (c) Frequency distributions of the circularity of cell outlines (WT, n = 280; + FtsZ1, n = 267; + FtsZ2, n = 534). (d) Western blots of whole cell lysates of the wild-type, FtsZ1 overproduction and FtsZ2 overproduction strains, probed with FtsZ1 or FtsZ2 antisera, as indicated. Total protein pre-staining of each membrane (with Ponceau S) is shown as a loading control.

Figure 5. Midcell localization of FtsZ1-mCh and FtsZ2-GFP. Mid-log cultures of (a) *H. volcanii* ID49 (WT + FtsZ1-mCh), (b) ID17 (WT + FtsZ2-GFP) and (d) ID67 (WT + FtsZ1-mCh + FtsZ2-GFP dual localization), cultured with 0.2 mM Trp, were imaged by phase-contrast and fluorescence microscopy. The mCh and GFP fluorescence was quantified along the long axis of cells, by plotting the relative (normalized) median intensity perpendicular to the long axis. (c) 3D-SIM images of *H. volcanii* ID16 (WT + FtsZ1-GFP) sampled during mid-log growth with 0.2 mM Trp. The upper two panels show a 'side-on' view (~70° tilt of the xy view), and the lower four panels show a ~20° xy tilt. (d) Co-localization of FtsZ1-mCh and FtsZ2-GFP fluorescence in cells, including selected examples of dividing cells (lower left). Correlation coefficients were plotted as a frequency distribution (80% of the cells had a correlation coefficient greater or equal to 0.7).

Figure 6. Localization interdependency and the effect of FtsZ mutations on FtsZ1-mCh and FtsZ2-GFP localization. Fluorescence and phase-contrast microscopy of mid-log *H. volcanii* strains (wild-type or Δ*ftsZ* backgrounds) carrying plasmid copies of the indicated *ftsZ* mutants and fusion proteins. Strains were grown with 0.2 mM Trp unless otherwise specified. Insets show either a magnified view at the arrowhead in the main panels (some with image channels separated), or another image acquired from cultures grown with the indicated concentration of Trp. (a) Localization of each FtsZ in the absence of the other FtsZ. (b) Localization of each FtsZ in the presence of the T7-loop mutant as the sole copy of the other. (c) Localization of each FtsZ in the wild-type background expressing the T7-loop mutant of the other. (d) The tagging of T7-loop mutants largely suppresses the dominant-inhibitory phenotype of the untagged proteins. (e) Strains similar to panel (b), except the T7-

loop mutant was also tagged. (f) As per panel (c), except the T7-loop mutant was also tagged (1 mM Trp data shown in the lower insets). Inset scale bars are 5 μm unless indicated otherwise.

Fig 1

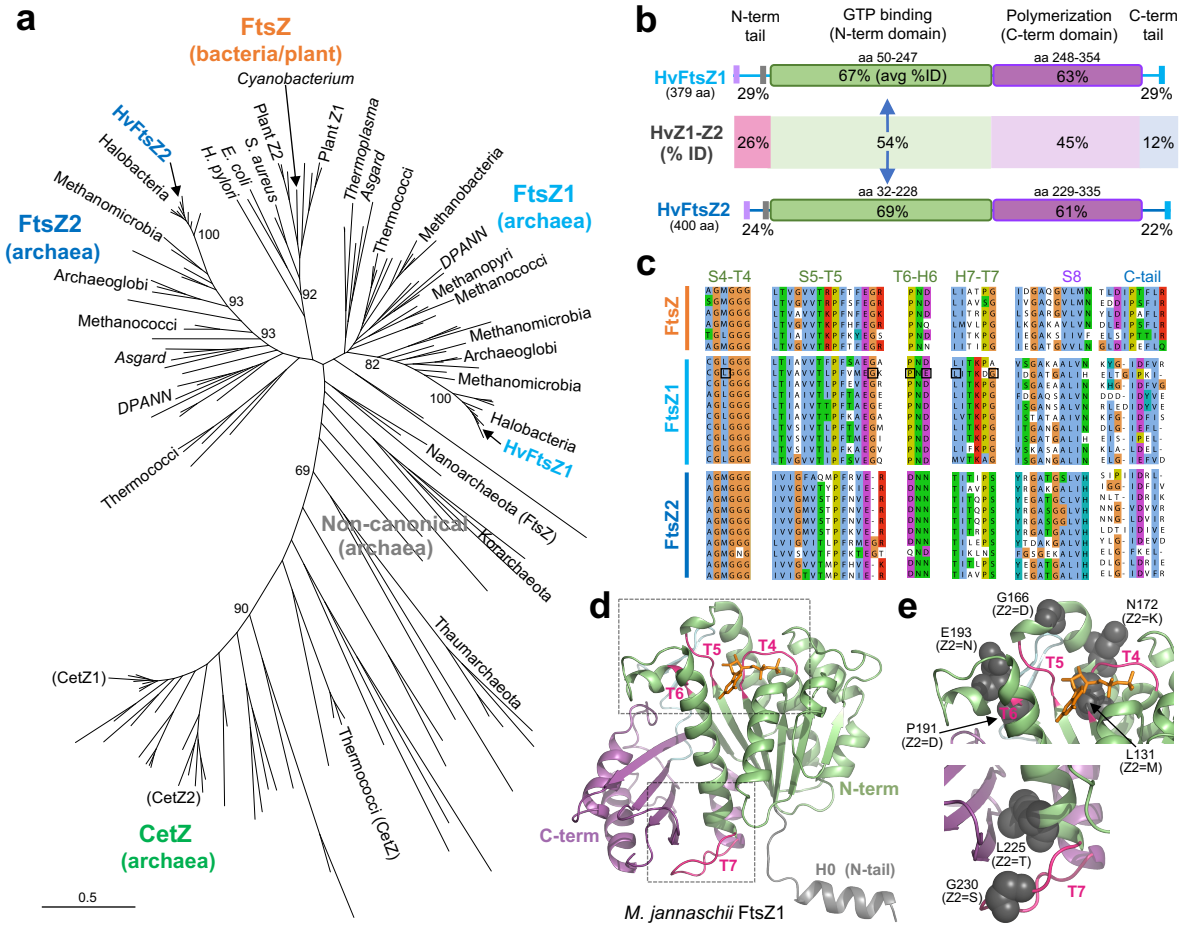
a
FtsZ
(bacteria/plant)
Cyanobacterium
Plant Z2
Plant Z1
S. aureus
E. coli
H. pylori
Thermoplasma
Asgard
Thermococci
Methanobacteria
DPANN
Methanopyri
Methanococci
Methanomicrobia
Archaeoglobi
Halobacteria
HvFtsZ2
FtsZ2
(archaea)
FtsZ1
(archaea)
Methanomicrobia
Archaeoglobi
Methanococci
Asgard
DPANN
Thermococci
Methanomicrobia
Halobacteria
HvFtsZ1
Nanoarchaeota (FtsZ)
Korarchaeota
Non-canonical
(archaea)
Thaumarchaeota
Thermococci (CetZ)
(CetZ1)
(CetZ2)
CetZ
(archaea)
100
93
92
93
82
100
69
90
0.5
b
N-term
tail
GTP binding
(N-term domain)
Polymerization
(C-term domain)
C-term
tail
HvFtsZ1
(379 aa)
aa 50-247
67% (avg %ID)
aa 248-354
63%
29%
29%
HvZ1-Z2
(% ID)
26%
54%
45%
12%
HvFtsZ2
(400 aa)
aa 32-228
69%
aa 229-335
61%
24%
22%
c
S4-T4
S5-T5
T6-H6
H7-T7
S8
C-tail
FtsZ
FtsZ1
FtsZ2
d
T5
T4
T6
N-term
C-term
T7
H0 (N-tail)
M. jannaschii FtsZ1
e
G166
(Z2=D)
N172
(Z2=K)
E193
(Z2=N)
T5
T4
T6
P191
(Z2=D)
L131
(Z2=M)
L225
(Z2=T)
G230
(Z2=S)
T7

Fig. 2

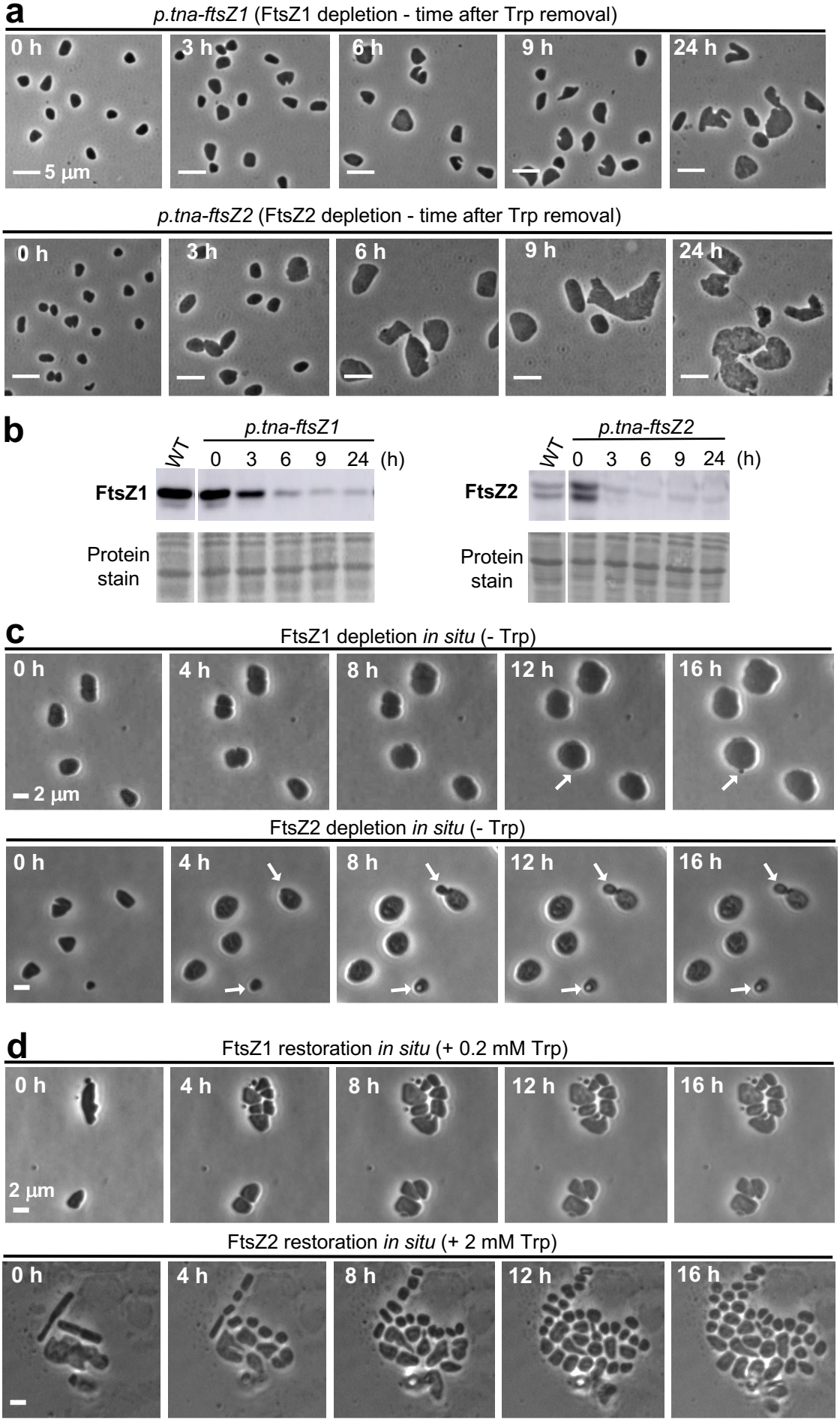
a
p.tna-ftsZ1 (FtsZ1 depletion - time after Trp removal)
0 h
3 h
6 h
9 h
24 h
5 μm
p.tna-ftsZ2 (FtsZ2 depletion - time after Trp removal)
0 h
3 h
6 h
9 h
24 h
b
p.tna-ftsZ1
WT
0 3 6 9 24 (h)
FtsZ1
Protein stain
p.tna-ftsZ2
WT
0 3 6 9 24 (h)
FtsZ2
Protein stain
c
FtsZ1 depletion in situ (- Trp)
0 h
4 h
8 h
12 h
16 h
2 μm
FtsZ2 depletion in situ (- Trp)
0 h
4 h
8 h
12 h
16 h
d
FtsZ1 restoration in situ (+ 0.2 mM Trp)
0 h
4 h
8 h
12 h
16 h
2 μm
FtsZ2 restoration in situ (+ 2 mM Trp)
0 h
4 h
8 h
12 h
16 h

Fig. 3

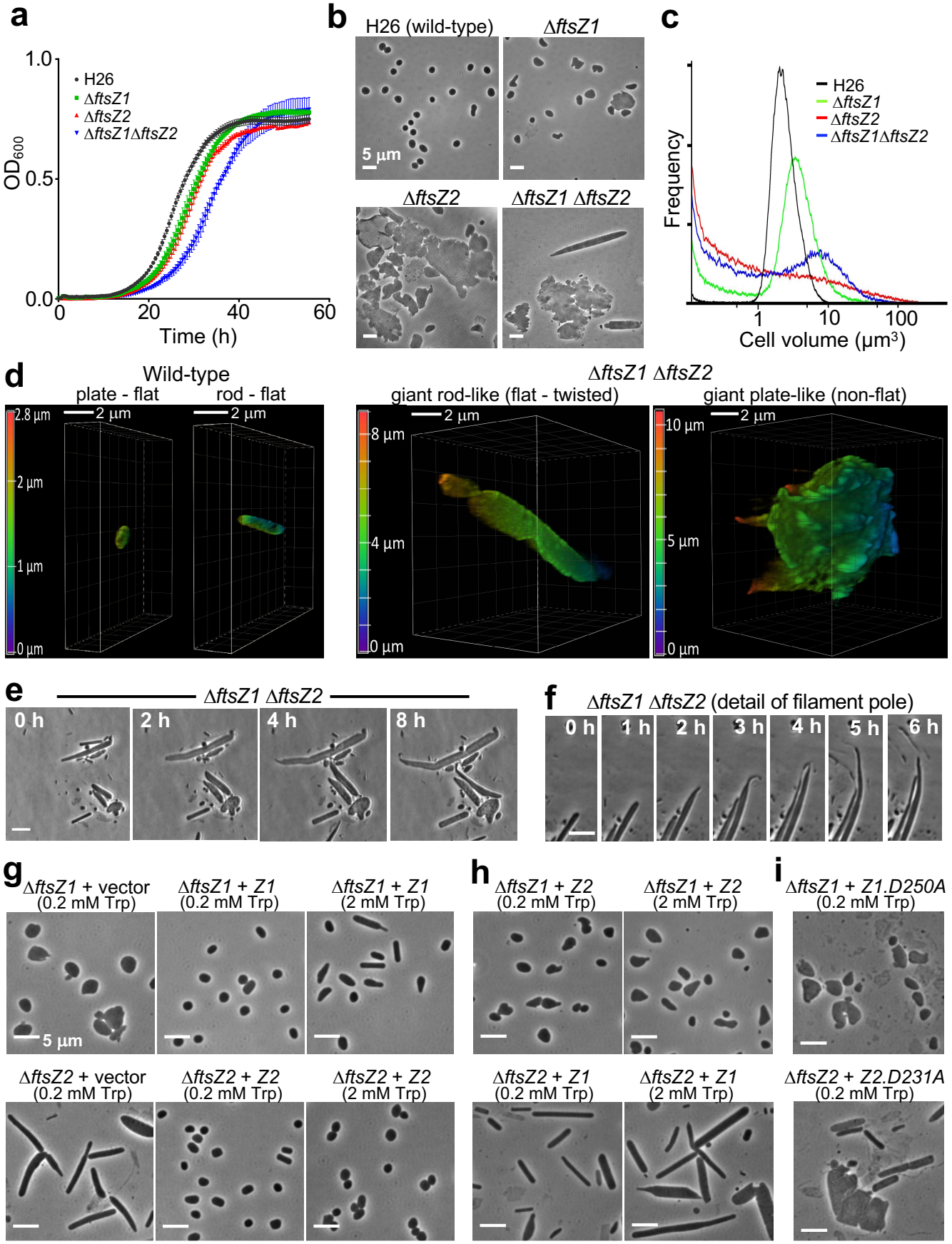
a
1.0
0.5
0.0
OD600
0
20
40
60
Time (h)
H26
ΔftsZ1
ΔftsZ2
ΔftsZ1ΔftsZ2
b
H26 (wild-type)
ΔftsZ1
5 µm
ΔftsZ2
ΔftsZ1 ΔftsZ2
c
Frequency
1
10
100
Cell volume (µm3)
H26
ΔftsZ1
ΔftsZ2
ΔftsZ1ΔftsZ2
d
Wild-type
plate - flat
rod - flat
ΔftsZ1 ΔftsZ2
giant rod-like (flat - twisted)
giant plate-like (non-flat)
2 µm
2.8 µm
1 µm
0 µm
8 µm
4 µm
10 µm
5 µm
e
ΔftsZ1 ΔftsZ2
0 h
2 h
4 h
8 h
f
ΔftsZ1 ΔftsZ2 (detail of filament pole)
0 h
1 h
2 h
3 h
4 h
5 h
6 h
g
ΔftsZ1 + vector (0.2 mM Trp)
ΔftsZ1 + Z1 (0.2 mM Trp)
ΔftsZ1 + Z1 (2 mM Trp)
5 µm
ΔftsZ2 + vector (0.2 mM Trp)
ΔftsZ2 + Z2 (0.2 mM Trp)
ΔftsZ2 + Z2 (2 mM Trp)
h
ΔftsZ1 + Z2 (0.2 mM Trp)
ΔftsZ1 + Z2 (2 mM Trp)
ΔftsZ2 + Z1 (0.2 mM Trp)
ΔftsZ2 + Z1 (2 mM Trp)
i
ΔftsZ1 + Z1.D250A (0.2 mM Trp)
ΔftsZ2 + Z2.D231A (0.2 mM Trp)

Fig. 4

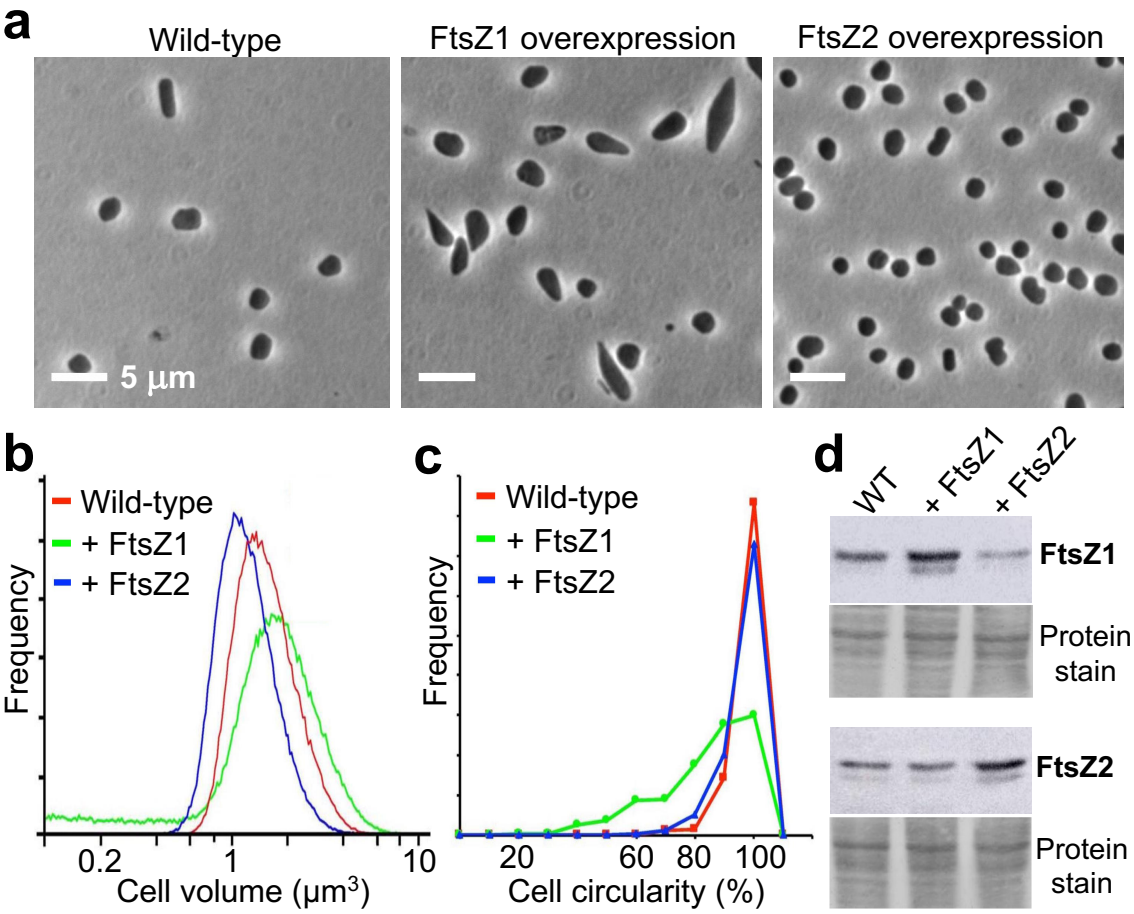
a
Wild-type
FtsZ1 overexpression
FtsZ2 overexpression
5 µm
b
Wild-type
+ FtsZ1
+ FtsZ2
Frequency
0.2
1
10
Cell volume (µm³)
c
Wild-type
+ FtsZ1
+ FtsZ2
Frequency
20
60
80
100
Cell circularity (%)
d
WT
+ FtsZ1
+ FtsZ2
FtsZ1
Protein stain
FtsZ2
Protein stain

Fig. 5

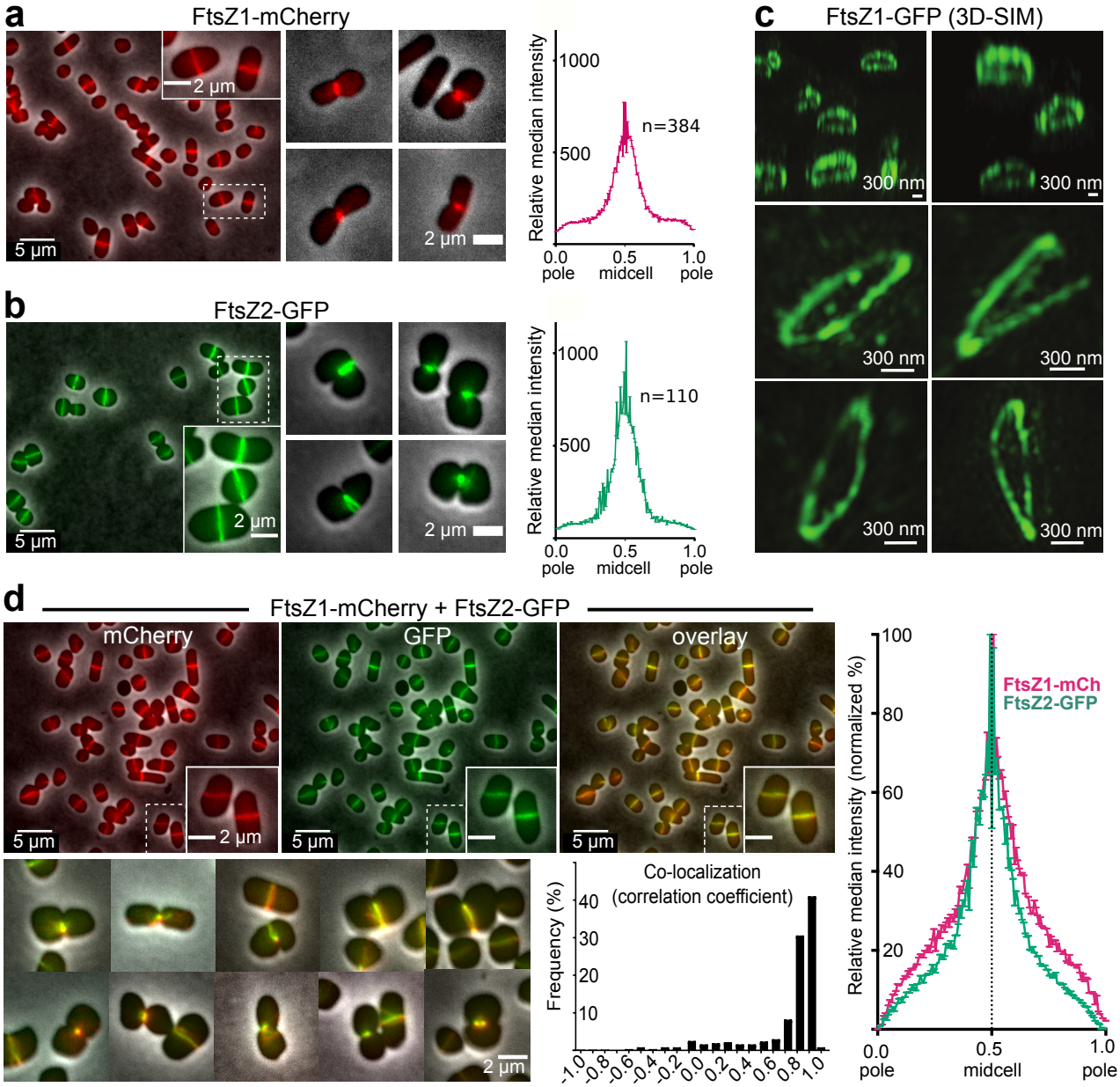
a
FtsZ1-mCherry
2 µm
5 µm
2 µm
Relative median intensity
1000
500
n=384
0.0
pole
0.5
midcell
1.0
pole
b
FtsZ2-GFP
5 µm
2 µm
2 µm
Relative median intensity
1000
500
n=110
0.0
pole
0.5
midcell
1.0
pole
c
FtsZ1-GFP (3D-SIM)
300 nm
300 nm
300 nm
300 nm
300 nm
300 nm
d
FtsZ1-mCherry + FtsZ2-GFP
mCherry
GFP
overlay
5 µm
2 µm
5 µm
5 µm
2 µm
Co-localization
(correlation coefficient)
Frequency (%)
40
30
20
10
-1.0
-0.8
-0.6
-0.4
-0.2
0.0
0.2
0.4
0.6
0.8
1.0
Relative median intensity (normalized %)
100
80
60
40
20
FtsZ1-mCh
FtsZ2-GFP
0.0
pole
0.5
midcell
1.0
pole

Fig. 6

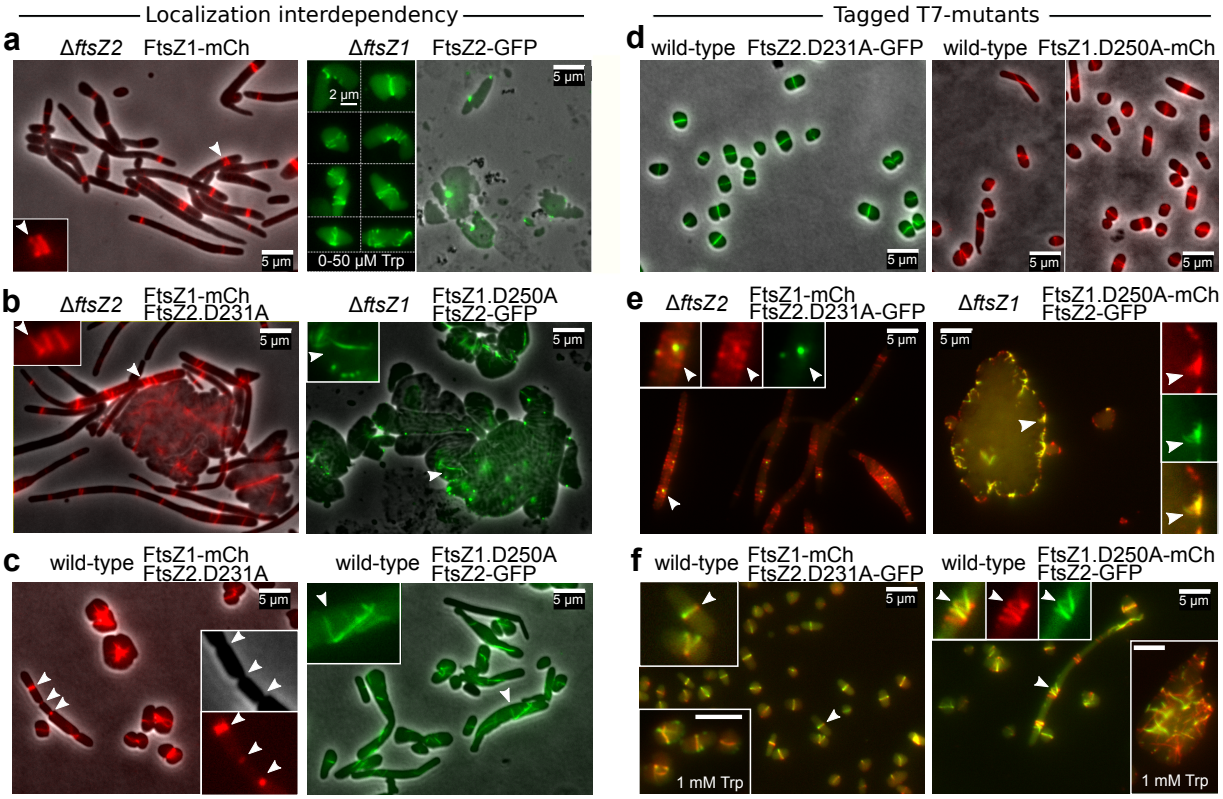
Localization interdependency
Tagged T7-mutants
a
ΔftsZ2 FtsZ1-mCh
ΔftsZ1 FtsZ2-GFP
2 µm
5 µm
0-50 µM Trp
b
ΔftsZ2 FtsZ1-mCh FtsZ2.D231A
ΔftsZ1 FtsZ1.D250A FtsZ2-GFP
c
wild-type FtsZ1-mCh FtsZ2.D231A
wild-type FtsZ1.D250A FtsZ2-GFP
d
wild-type FtsZ2.D231A-GFP
wild-type FtsZ1.D250A-mCh
e
ΔftsZ2 FtsZ1-mCh FtsZ2.D231A-GFP
ΔftsZ1 FtsZ1.D250A-mCh FtsZ2-GFP
f
wild-type FtsZ1-mCh FtsZ2.D231A-GFP
wild-type FtsZ1.D250A-mCh FtsZ2-GFP
1 mM Trp